Check for updates

Geochemistry, Geophysics, Geosystems

RESEARCH ARTICLE
10.1029/2020GC009202

Key Points:

- Tonalitic migmatites show distinct deformation signatures and seismic properties during pre-, syn-, and post-migmatization
- Power-law creep dominates solid phases' deformation, near-Newtonian flow is typical for deformation in rocks with high melt content
- Migmatites have low Vs and extreme high seismic anisotropies in the syn-melt condition

Supporting Information:

- Supporting Information S1

Correspondence to:
Y. Liu,
liuyongjiang@ouc.edu.cn

Citation:
Shao, Y., Piazolo, S., Liu, Y., Lee, A. L., Jin, W., Li, W., et al. (2021). Deformation behavior and inferred seismic properties of tonalitic migmatites at the time of pre-melting, partial melting, and post-solidification. *Geochemistry, Geophysics, Geosystems*, *22*, e2020GC009202. https://doi.org/10.1029/2020GC009202

Received 29 MAY 2020
Accepted 18 JAN 2021

© 2021. American Geophysical Union. All Rights Reserved.

Deformation Behavior and Inferred Seismic Properties of Tonalitic Migmatites at the Time of Pre-melting, Partial Melting, and Post-Solidification

Yilun Shao[1], Sandra Piazolo[2,3], Yongjiang Liu[4,5], Amicia L. Lee[6], Wei Jin[7], Weimin Li[7], Chenyue Liang[7], and Quanbo Wen[7]

[1]Department of Geology, University of Otago, Dunedin, New Zealand, [2]School of Earth and Environment, University of Leeds, Leeds, UK, [3]Australian Research Council of Excellence for Core to Crust Fluid Systems/GEMOC, Department of Earth and Planetary Sciences, Macquarie University, Sydney, NSW, Australia, [4]Frontiers Science Center for Deep Ocean Multispheres and Earth System, Key Lab of Submarine Geosciences and Prospecting Techniques, MOE and College of Marine Geosciences, Ocean University of China, Qingdao, China, [5]Laboratory for Marine Mineral Resources, Qingdao National Laboratory for Marine Science and Technology, Qingdao, China, [6]Department of Geosciences, University of Tromsø, Tromsø, Norway, [7]College of Earth Sciences, Jilin University, Changchun, Jilin, China

Abstract As seismic data from the lower crust becomes more readily available, it is important to link seismic properties to the ongoing processes within lower crustal evolution. This includes high temperature, pre- and post-migmatization solid state deformation as well as melt-present deformation. We selected two tonalitic migmatites with variable former melt content (one metatexite and one diatexite) from the lower crustal Daqingshan area, northern North China Craton to assess the link between seismic properties and rock structure and rheology. Field observation along with microstructural features suggest that the characteristics of hornblende and plagioclase within the residuum of the metatexite can be used to derive information on the pre-melt deformation. Residuum's plagioclase CPO (crystallographic preferred orientations) is consistent with high temperature dislocation creep as the main deformation mechanism; similarly, hornblende shows a strong CPO related to dislocation creep. During syn-melt (melt present) conditions, phenocrysts of plagioclase in the metatexite's neosome and K-feldspar and peritectic hornblende in the diatexite's neosome are present. The rheology of the rock was dominated by melt; hence is inferred to follow Newtonian flow. After melt crystallization deformation is minor but again dominated by dislocation creep. The seismic properties (seismic velocity, anisotropy, Vp/Vs ratio, etc.) for pre- and post-melt have similar values expected values for solid mafic rocks, whilst the syn-melt seismic velocities are generally lower and Vp/Vs ratios and seismic anisotropies are higher.

1. Introduction

The rheological behavior of the lower crust is still under continuous debate (e.g., jelly sandwich, crème brûlée and banana split; Bürgmann & Dresen, 2008; Burov & Diament, 1995; Jackson, 2002), while the geophysical information is of pivotal importance to our understanding of lithospheric flow behavior governing the lower crust of orogenies (Almqvist & Mainprice, 2017; Bürgmann & Dresen, 2008; Rudnick & Fountain, 1995). Migmatites are one of the main rock type in the lower crust, hence it is important to investigate the related deformation process to infer the rheological evolution of the lower crust (Hasalová et al., 2008; Vanderhaeghe & Teyssier, 2001). Understanding deformation mechanisms and geophysical implications of the two main stages of migmatization, partial melting and rock solidification, are essential to recover lower crust evolution and its rheology (Almqvist & Mainprice, 2017; Almqvist et al., 2015; Dell'Angelo & Tullis, 1988; Gómez Barreiro et al., 2007; Miranda & Klepeis, 2016). Generally, the domain that is slightly influenced by partial melting preserves predominantly the rock's geological history before melting (referred to as residuum; Guernina & Sawyer, 2003; Sawyer, 2008). In contrast, the neosome (also referred to as leucosome, melanosome, etc.) represents the former melt-dominated area (Kriegsman, 2001; Kriegsman & Hensen, 1998; Sawyer & Brown, 2008). In addition, granitoid rocks (e.g., granite, diorite, tonalite) in the partial melting condition would generate K-feldspar and quartz (Barker & Arth, 1976; Barker et al., 1981; Tuttle & Bowen, 1958).

During partial melting in the lower crust, the deformation behavior of a rock is primarily determined by the melt fraction and its distribution. At low melt fractions (2%–4%), dislocation creep (e.g., grain boundary

migration [GBM]) may be active (Walte et al., 2005; Závada et al., 2007). As the melt fraction increases to approximately 7%, grain boundary sliding (GBS) is activated, and usually diffusion creep dominant (Cooper & Kohlstedt, 1984; Hasalová et al., 2008; Závada et al., 2018). When the melt fraction is greater than 8%, granular flow plays a major role (Paterson, 2001; Walte et al., 2005). Microscopic observations show that melt may be trapped at grain triple junctions (Cooper & Kohlstedt, 1984; Sawyer, 2001; Walte et al., 2005; Závada et al., 2007) or form a connected melt network along grain boundaries (Dell' Angelo & Tullis, 1988; Stuart et al., 2017, 2018). At high melt fractions (e.g., >10%), melt can segregate and the rheological behavior of the bulk rock is dominated by the shape of the melt (e.g., Newtonian; Burg & Vigneresse, 2002; Champallier et al., 2008; Rosenberg & Handy, 2005). Miranda and Klepeis (2016) indicate that lower crust rocks that have previously undergone partial melting and melt solidification may deform by solid-state dislocation creep during further deformation events. In contrast, microstructural analysis of migmatites during a single deformation event only develop weak post-crystallization and solid-state deformation characteristics in the "crystallized melt" portion of the rock (Prakash et al., 2018). Consequently, in the latter case the protolith (or residuum in this case study) takes up most of strain-related deformation (Franěk et al., 2011; Vanderhaeghe, 2009). Seismic properties of lower crustal rocks are influenced by not only mineral modal content (Lloyd et al., 2011; Rudnick & Fountain, 1995), but also by metamorphic banding (Cyprych et al., 2017) and constituent minerals' (e.g., hornblende and biotite) crystallographic preferred orientations (CPO) (Lloyd et al., 2011; Tatham et al., 2008). Melt production decreases both P-wave (Vp) and S-wave (Vs) velocities, and the large decrease in Vs leads to high Vp/Vs (Almqvist et al., 2015; Ferri et al., 2016; Hammond & Humphreys, 2000; Schilling & Partzsch, 2001). Consequently, seismic low-velocity zones are inferred to represent zones of partial molten lower crust (Caldwell et al., 2009; Lee et al., 2017; Xie et al., 2013). During partial melting, seismic anisotropy can be increased by layered melt or crystallographic orientation of minerals (Almqvist et al., 2015; Holtzman & Kendall et al., 2010), and decreased by breakdown of highly anisotropic minerals (e.g., micas) or the distribution of melt in tubes (Ferri et al., 2016; Hacker et al., 2014). In addition, studies have shown that the Vp/Vs ratio may be useful to infer the degree of partial melting (Ferri et al., 2016; Lee et al., 2017; Nábelek et al., 2009). For example, it has been suggested that when Vp/Vs ≈ 2 there may be partial melting at intermediate depth (Julià et al., 2005). Hacker et al. (2014) established a model to predict seismic velocities in partially molten rocks in Central Tibet (Qiangtang block), suggesting that the low shear wave velocity (~3.3 km/s) may be due to melt injection from the deeper crust. Studies of seismic properties of post-migmatization lower crustal rocks are rare. Hacker et al. (2014) showed in their model that crystallized melt is expected to decrease Vs, with seismic properties mimicking that of partially molten rocks.

Over the last 20 years, electron backscatter diffraction (EBSD) analysis (Prior et al., 1999; Venables & Harland, 1973) has enabled determination of the CPO of minerals in a rock. The CPO has been applied to calculate seismic properties (Mainprice, 1990; Mainprice et al., 2011), and it is possible to infer the geophysical properties of a rock specimen (Almqvist & Mainprice, 2017; Cyprych et al., 2017; Ferré et al., 2014; Lamarque et al., 2016; Lloyd et al., 2011; Tatham et al., 2008). So far, research computing seismic responses (e.g., velocity, anisotropy, Vp/Vs ratio, etc.) from natural examples has utilized data from a whole rock (Hacker et al., 2014; Rudnick & Fountain, 1995). In the case of a migmatites, different domains have their own physical properties that should be considered in order to decipher the seismic signals at the different stages of the rock's history (i.e., protolith prior to melting, partial melting, migmatization, melt frozen, etc.). Hence, assessing the properties of the different parts of the migmatite would allow for an improvement of our ability to link seismic characteristics to partial melting and/or melt frozen status. Since different degrees of melting occur in the lower crust (Sawyer, 2014; Vanderhaeghe, 2001), exploring the effect of such different melt fractions within the same rock type is important (Lee et al., 2017). To improve our ability to assess seismic data in the light of absence, presence or former presence of melt, it is important to assess the evolution of seismic properties of a migmatitic unit taking its properties pre-, syn- and post-melting into account. Consequently, in this study we investigate the behavior of a migmatites before, during and after melting. In particular, we focus on: (1) the deformation characteristics and deformation evolution in different migmatite domains of two rock samples with differing former melt fractions; (2) the rheological behavior through their geological evolution; and (3) the seismic signature during partial melting and post-melting, in the melt-frozen status.

2. General Geological Setting

The study area, Daqingshan, was chosen as it exhibits migmatitic rocks without significant retrograde overprinting, making it an ideal field location to study lower crustal migmatites. The study area lies in the middle "Khondalite Belt" between Yinshan Block and Ordos Block, which constitute the main part of the Western Block of northern North China Craton (NCC; Guo et al., 2012; Santosh et al., 2007, 2009; Zhao & Guo, 2012; Zhao et al., 2005, 2012; Figure 1a inset). The current model for the evolution of NCC is that Yinshan and Ordos Block amalgamated along the E-W trending Khondalite Belt during a Precambrian event (1.95–1.92 Ga) forming the Western Block. Around 1.85 Ga the Trans-North China Orogen (TNCO) was formed by collision with the Eastern Block (Zhao, 2007; Zhao et al., 2002, 2005, 2012; Figure 1a inset). The high-grade Khondalite Belt is associated with the latter collision. It is dominated by metasediments with subvertical foliation (Figure 1b) and several E-W trending steep ductile shear zones (Gong et al., 2014; Yang et al., 2008).

The Daqingshan area is dominated by a series of Precambrian metamorphic rocks from Late Neoarchean to Late Paleoproterozoic. It mainly includes metamorphosed Trondhjemite-Tonalite-Granodiorite (TTG, around 2.5 Ga), mafic granulite (metamorphic gabbro, Sanggan Group, Late Neoarchean), banded gneiss (Lower Wulashan Group, Late Archean-Early Paleoproterozoic), metasediments (Upper Wulashan Group or Khondalite series, Late Paleoproterozoic), Daqingshan supracrustal rocks (2.50–2.45 Ga), and granitic gneiss (Late Paleoproterozoic) (Dong et al., 2014; Jin et al., 1991, 1992; Ma, Wan, Santosh, et al., 2012; Ma, Wan, Xu, et al., 2012; Wan et al., 2009, 2013; Xu et al., 2007, 2015; Yang et al., 2008; Figure 1). From north to south, the migmatites have been shown to become increasingly hotter (~647 to ~920 °C) exhibiting an increasing amount of melt signature at peak metamorphism, however little or no pressure difference is documented (Figures 1 and 2; Cai et al., 2014; Cai, Liu, Liu, Liu, et al., 2013; Cai, Liu, Liu, Shi, et al., 2013). Previous studies interpret a N-S increase in the degree of local melting with a peak in the southern sample area (near Xuehaigou), where flow features are common and thick bands of felsic material are ubiquitous in outcrop (Figure 2; Ma, Wan, Xu, et al., 2012; Xu et al., 2015). The studied profile represents the root of Paleoproterozoic orogeny, deepening from north to south. The recorded pressure-temperature conditions indicate that the migmatization occurred at 20–30 km depth within a collisional orogen which may have been overthickened (Corona-Chávez et al., 2006; Lobjoie et al., 2018; Ray et al., 2009). Our samples therefore originate from the deep mid-crust or lower crust; hence their analyses contribute to the understanding of rheology and signature of such rocks. In the following, for simplicity we refer to our samples as lower crustal rocks.

3. Definition of Terms and Methods

3.1. Definition of Terms

The term migmatite defines that a rock has at least two petrographically different parts, which are influenced by presence of melt in medium-high grade metamorphic environments (Kriegsman, 2001; Maxeiner et al., 2017; Olsen, 1977). We follow Sawyer & Brown (2008) and define the parts that experienced partial melting as "residuum" domains. In this case study, residuum domains are comprised of non-melt minerals and minor crystallized melt. The parts with solid phase and abundant crystallized melt are dominated by either felsic minerals (leucosome) or dark minerals (melanosome) (Figure 3; Johannes & Gupta, 1982; Kriegsman & Hensen, 1998; Kriegsman, 2001), which we term the "neosome" (Olsen, 1977; Sawyer et al., 2011). Based on the definitions above, we assume that in a single migmatite sample, the residuum domain has stronger deformation characteristics than the neosome domain, and within the neosome, the solid phase has stronger deformation characteristics than crystalized melt. In this contribution the melt fraction is used to divide sampled migmatites into metatexite (<26 melt%) and diatexite (>26 melt%) (based on Sawyer & Brown, 2008).

3.2. Sample Selection and Preparation

To explore the deformation behavior and seismic properties of typical lower crustal migmatites, we selected two representative samples of broadly tonalitic composition with a general assemblage of hornblende, pla-

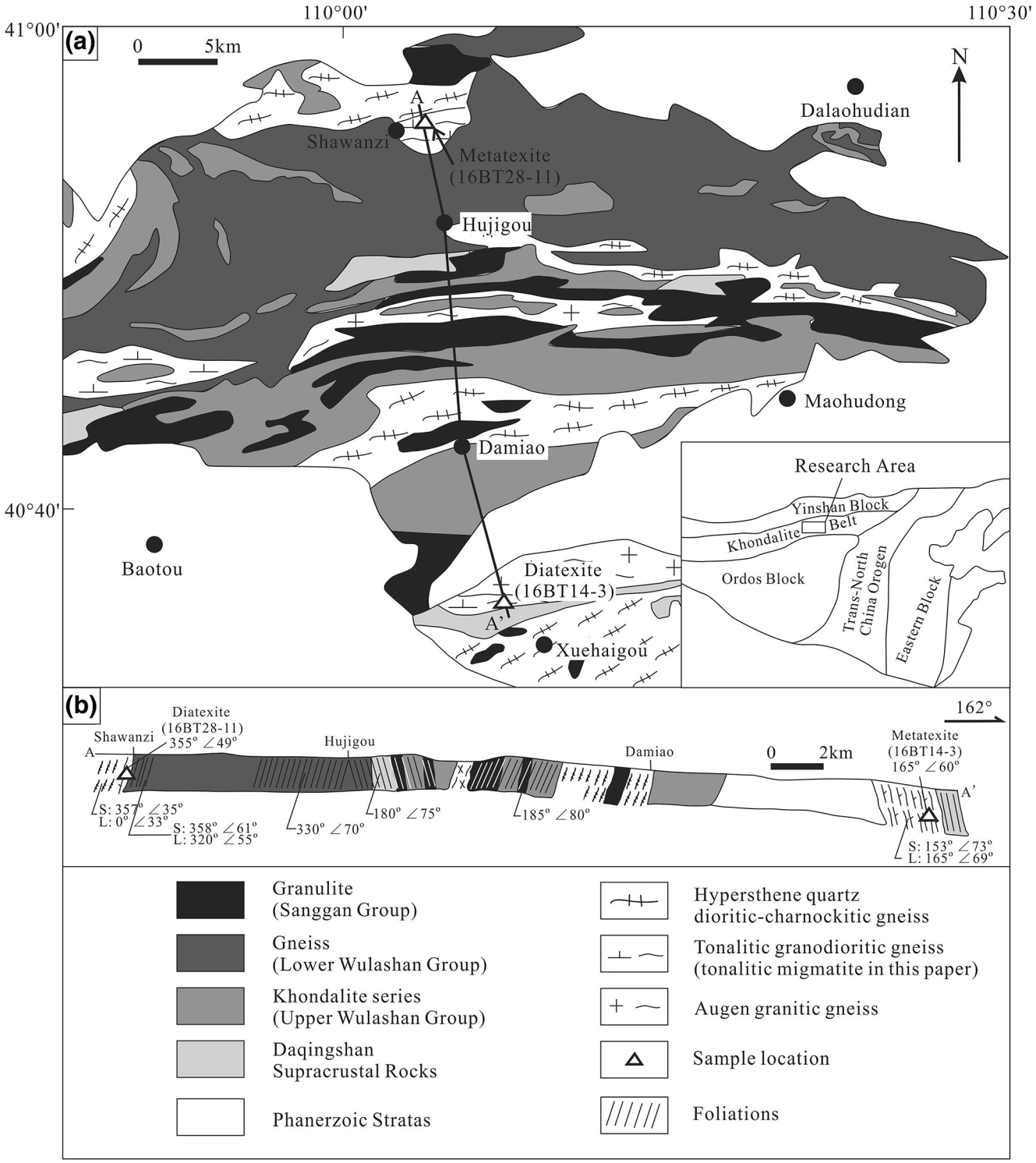

Figure 1. Geological map (a) with a simplified cross-section along A-A′ (b) in the Daqingshan area, inset reveals the location in North China Craton (NCC), modified from Zhao et al. (2005), Xu et al. (2007), and Wan et al. (2013). Numbers refer to selected samples' azimuth with dip of foliation (S) and plunge of lineation (L). Sample localities are also marked.

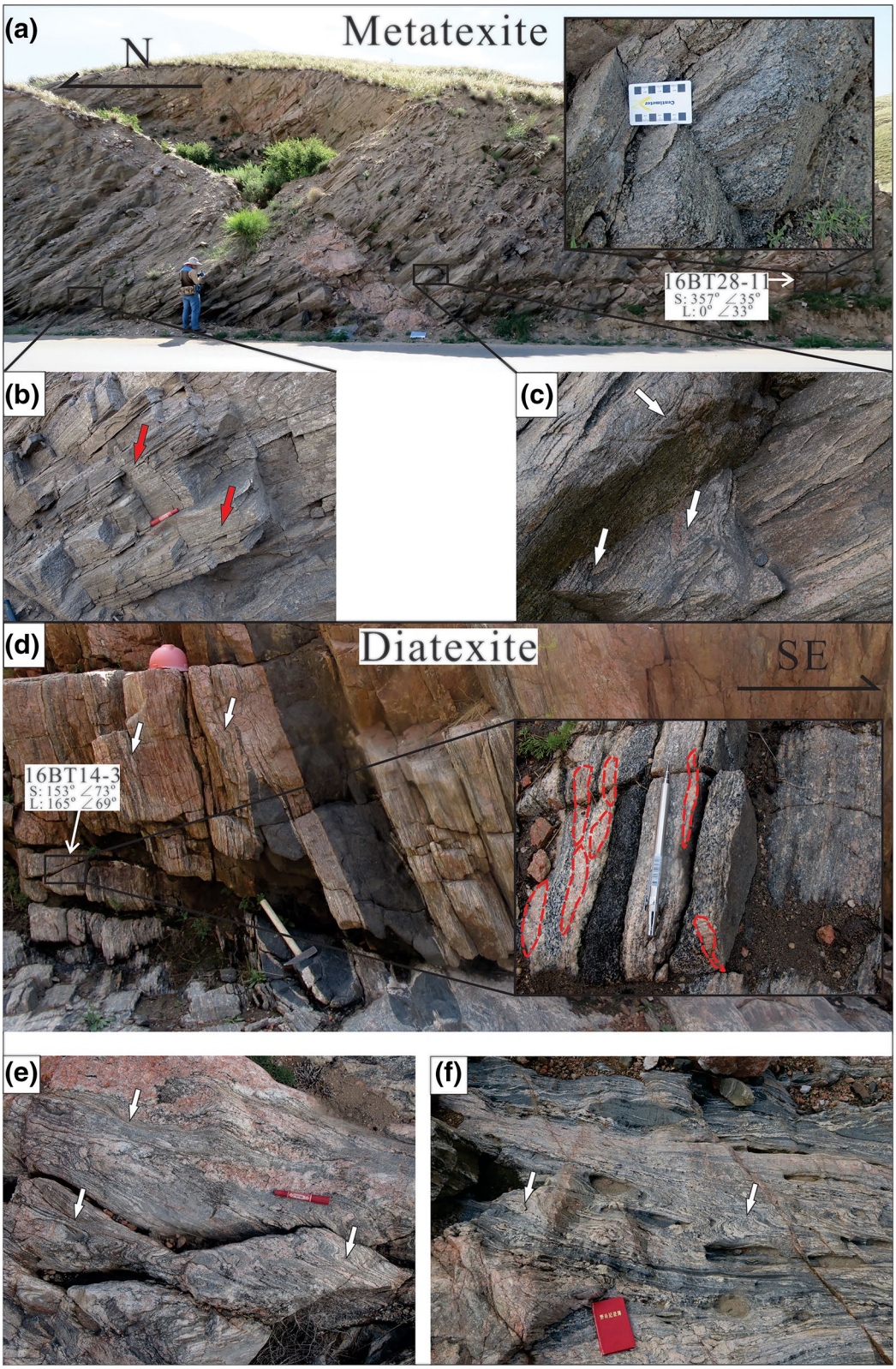
(a)
N
Metatexite
16BT28-11
S: 357° ∠35°
L: 0° ∠33°
(b)
(c)
(d)
Diatexite
SE
16BT14-3
S: 153° ∠73°
L: 165° ∠69°
(e)
(f)

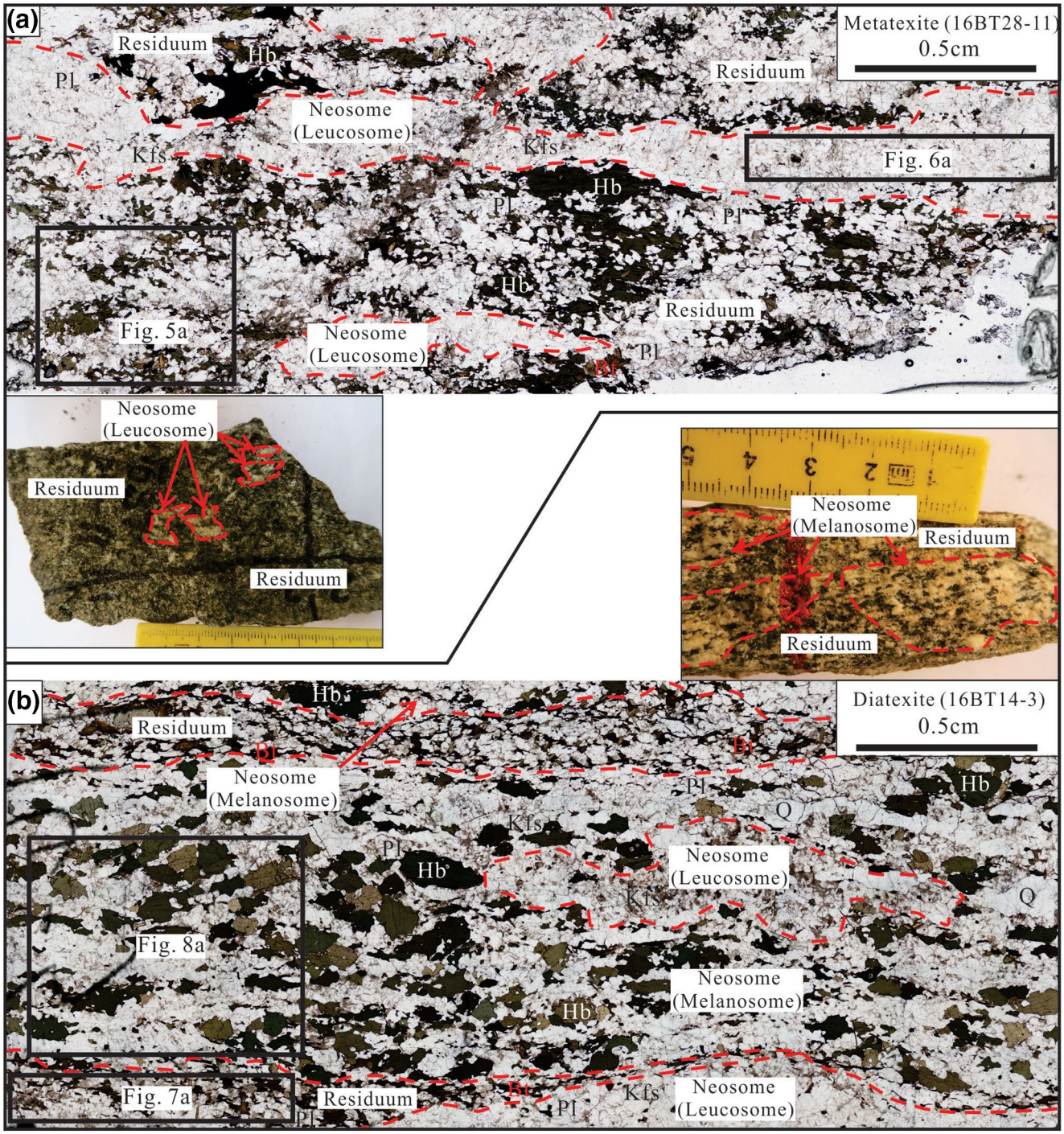

Figure 3. Oriented thin section microphotographs (plane-polarized light) and hand specimen photographs of tonalitic migmatites; (a) metatexite and (b) diatexite; residuum and neosome (leucosome or melanosome) domains are labeled and boundaries shown as red dashed lines; black rectangles show location of the EBSD map areas.

Figure 2. Outcrop characteristics of tonalitic migmatite sampled in northern (metatexite, a–c) and southern research area (diatexite, d–f); (a) profile near Shawanzi; (b) banded layers; (c) stromatic (thin, parallel and laterally persistent layers) to net (oriented felsic layers outline polygonal darker rock) layers; (d) profile near Xuehaigou with syn-tectonic character (more stromatic layers, oblate shapes in enlarged photo); (e) and (f) are outcrops with numerous anatectic features (e.g., stromatic). Red arrows: band features; white arrows: flow features; red dashed lines: profile of oblate felsic rock areas. Numbers refer to selected samples' azimuth and dip of foliation (S)/plunge of lineation (L).

gioclase, K-feldspar and minor quartz (Figure 1 and Table 1). The two samples represent migmatites with different amounts of leucocratic material, which is inferred to represent former (now crystallized) melt (Figures 1 and 2). We chose to study tonalitic migmatites as it is a typical lower crust rock in orogens (Sawyer, 1996; Weinberg et al., 2015). Both samples have well-developed LS fabric on the mm to cm scale. The leucocratic material has an oblate to flattened ellipsoid shape with the longest axis parallel to the lineation and the shortest axis perpendicular to the foliation (Figures 2 and 3), a signature of plane strain deformation. Polished thin sections were prepared from blocks cut perpendicular to the foliation (XY section) and parallel to lineation (X axis).

General textural information such as grain shape, mineral assemblages and optical characteristics were collected using a petrographic microscope. Prior to EBSD and energy-dispersive X-ray spectroscopy (EDS) analyses the sections were polished using mechano-chemical colloidal silica and coated with carbon (~3 nm). A thicker carbon coat (~10 nm) was applied for the separate microchemical maps attained by electron microprobe.

3.3. Quantitative Crystallographic Orientation Analysis—EBSD

Quantitative crystallographic orientation data was obtained by using EBSD 3D orientation data (Prior et al., 1999), collected in the Geochemical Analysis Unit (GAU), Macquarie University on a Zeiss IVO SEM (Scanning Electron Microscopy) with a Nordlys Nano High sensitivity EBSD detector and an X-Max EDS detector to ensure a high quality EBSD and chemical data. The latter data was required to ensure correct identification of the feldspar phases. Analysis conditions were high vacuum, 20 kV acceleration voltage, beam current of 8.0 mA, and at a working distance of ~12 mm. EBSD maps were collected with a step size of 15 μm. Grains are defined as areas completely surrounded by high angle boundaries (misorientation ≥10°) and comprised of at least 4 data points. Boundaries with misorientations of 2–10° are defined as subgrain boundaries (Pearce et al., 2011; Trimby et al., 2000; Warren & Hirth, 2006). Grains with an average internal misorientation <1° are considered as strain-free (Piazolo et al., 2006). Noise reduction on the raw data followed methods tested by Bestmann and Prior (2003), Piazolo et al. (2006), and Prior et al. (2002). Orientations are plotted in equal area, lower hemisphere pole figures (one point per grain), half width 20° and cluster size 5° to investigate the presence and/or absence of CPO (Law, 1990; Menegon et al., 2011). Misorientation axes (MXD) data are shown in equal area and upper hemisphere inverse pole figures, and the axes value divided by valid grain (>65 μm) amounts (i.e., MXD axes/grain amounts ratio, see Table 1 for detail) will be used to detect mineral's deformation degree. Misorientation angle distributions are presented for neighbor and random pairs (also known as correlated and uncorrelated data). For comparison, we also provide the theoretical frequency distribution curve for a random orientation distribution as a black line. It should be noted that misorientation angle distributions diagrams are influenced by the known plagioclase twin relationships with high neighbor-pair frequencies at 170°–180° (Figures 5c, 6c, 7c, and 8c). For quartz this is also the case for 60° signifying the presence of Dauphine twins. In addition, GOS (grain orientation spread) is computed, this represents average deviation of the orientation of a measurement point from the average orientation of the grain (cf. Wright et al., 2011, for a review). Considering the geological conditions and sample properties, we concentrated our analysis on plagioclase, K-feldspar and hornblende (>10%) in each domain (i.e., residuum or neosome). Additionally, we used J-index for the minerals' long <c> axis as a measure for CPO strength and computed the average angle of the long grain shape axis relative to the foliation plane. The GOS and J-index data sets are calculated using the MTEX Matlab toolbox by using orientation data from EBSD (Mainprice et al., 2011, 2014).

4. Results

4.1. Field Relationships and General Sample Description

The metatexite sample comes from the east side of Shawanzi (N:40°54′03”, E: 110°04′10”; Figure 1). The gneiss dips northward and exhibits a large number of 0.5–1.5 m wide, felsic veins (Figures 1b and 2a), banded gneiss (tonalite with granitic injection; Figure 2b) and stromatic to “net” migmatitic structure (Fig-

Geochemistry, Geophysics, Geosystems

10.1029/2020GC009202

Table 1
General Information of the Two Studied Tonalitic Migmatites

Anatectic type	Total rock-forming minerals	EBSD measured domain	Mineral	Modal percent %	Pl/Kfs ratio	Number of grains	Average grain size d/μm	Aspect ratio	GOS/°	J-index	Angle between long axis and horizontal/°	MXD axis	MXD axes/grain amount
Metatexite (16BT28-11)	Pl (58.0%)	Residuum (70%)	Pl	66.5	9.64	758	186	1.56	0.75	3.15	−4.76	1239	1.63
	Kfs (21.7%)		Kfs	6.9									
	Hb (14.3%)		Hb	20.0		352	148	1.78	0.73	9.34	−7.11	743	2.11
	Q (3.5%)					(5)	(657)	(2.10)					
	Bt (2.5%)		Q	3.2									
			Bt	3.4									
		Neosome (30%)	Pl	39.5	0.72	252	162	1.69	0.58	7.91	−0.79	466	1.85
			Kfs	54.5		300	176	1.65	0.55	6.49	0.27	300	1.00
			Hb	1.6									
			Q	4.4									
Diatexite (16BT14-3)	Pl (32.4%)	Residuum (15%)	Pl	64.1	4.27	221	166	1.69	0.43	13.4	15.61	70	0.32
	Kfs (13.8%)		Kfs	15.0		74	122	1.59	0.46	10.7	18.02	48	0.65
	Hb (33.8%)		Q	11.8									
	Q (18.3%)		Bt	9.1									
	Bt (1.7%)	Neosome (85%)	Pl	29.7	2.20	519	175	1.71	0.33	4.09	21.34	153	0.29
			Kfs	13.5		309	149	1.65	0.51	4.79	21.09	176	0.57
			Hb	37.8		214	257	1.81	0.4	8.51	21.09	338	1.58
						(33)	(743)	(2.03)					
			Q	18.9									

Note. Total Rock-forming Minerals Stand for Minerals in One Sample's All Measured Domains (Percentages Mean Total Mineral Modal Content), Modal Percent and Feldspars' Ratio, Valid Grain Amounts, Grain Size, Aspect Ratio, GOS, J-index, Angle between Long Axis and Horizontal, MXD Axis Amounts and MXD Axes/grain Amounts Ratio Information are All Based on EBSD data, Hornblende's Microstructural Data inside Brackets Represent Porphyroblastic Grains (larger than 500 μm). Mineral Abbreviations Used Follow Kretz (1983).

Abbreviations: Bt, biotite; Hb, hornblende; Kfs, K-feldspar; Pl, plagioclase; Q, quartz.

ure 2c). The diatexite is collected near Xuehaigou in the southern part of the study area (N:40°37′32”, E: 110°06′05”; Figure 1), where felsic migmatites are exposed and characterized by 3–5 cm wide felsic (feldspars and quartz) bands (Figure 2d). The local gneiss is injected by mafic dykes that are now metamorphosed to mafic granulite with subsequent melt injections (Figure 2d). The felsic migmatite in this area exhibits flow structures (e.g., schlieren structures) surrounding rigid mafic blocks (Figures 2e and 2f).

Sample 16BT28-11 represents a metatexite with separated residuum and neosome (leucosome) domains (Figure 3a and Table 1). In hand specimen the felsic material makes up 15%–20% of the sample. Individual leucocratic areas have an oblate to flattened ellipsoid shape with the longest axis parallel to the lineation (Figure 3a). The residuum is dominated by hornblende and plagioclase, where hornblende grains are parallel to the lineation. The neosome is dominated by felsic minerals (mainly K-feldspar with subordinate plagioclase) and the domain is vein-shaped and subparallel to the foliation and injects the residuum (Figure 3a and Table 1).

Sample 16BT14-3 represents a diatexite, which is dominated by neosome. The shape of the neosome defines a wavy foliation exhibiting an elongate ellipsoidal to oblate shape (Figure 3b). The residuum plagioclase grains are associated with lineation-parallel biotite (Figure 3b). K-feldspar takes up 15% of the residuum, higher in abundance than in the metatexite's residuum. The neosome forms larger areas in thin section (Figure 3b), with K-feldspar making up 13.5% of this region (Table 1). Hornblende is the main mineral of the diatexite's neosome (37.8%), the long axis of grains is commonly inclined to the general foliation (∼17–22°; Figure 3b and Table 1).

4.2. Microstructural Characteristics in Migmatites

In the metatexite, plagioclase (66.5%) is the dominant mineral of the residuum (Table 1). The grains are equigranular with an equant grain shape, curved grain boundaries and also polygonal with abundant 120° triple junctions (Figures 4a and 5a). The average grain size is 186 μm with a low mineral aspect ratio (1.56) (Table 1). Hornblende grains in the residuum exhibit a shape preferred orientation fabric (SPO; Figure 3a). The grains have porphyroclast (>500 μm; 5 grains) or anhedral grain shapes (Figures 3a and 5b) with brittle intergrain fracturing (Figure 4b). The total grain size variation is large due to the porphyroblasts but the smaller anhedral grains dominate the domain (Figures 3a and 5a and Table 1). Equilibrium triple junctions are frequent in areas abundant with hornblende and minor biotite locally occurs at hornblende boundaries (Figure 4b). The average aspect ratio of hornblende (1.78) is significantly higher than plagioclase (Table 1). For the subordinate minerals, K-feldspar grains are dispersed in the residuum domain with subhedral shapes, quartz grains are elongate and occur mainly as interstitial material (Figure 6a). Plagioclase in the neosome domain shows a similar grain size range, shape, and aspect ratio as in the residuum, except that the mean grain size is smaller (162 μm). K-feldspar in the neosome has similar features as plagioclase in the same domain (Table 1 and Figures 4c and 6a) and myrmekite textures are observed adjacent to plagioclase (Figure 4a). Hornblende is also present in the neosome and surrounded by plagioclase clusters (Table 1 and Figures 4c, 6a, and 6e). Quartz has low abundance (less than 5%; Table 1) in both domains and either forms elongated grains (Figure 5a) or occurs as interstitial grains surrounded by feldspar (Figures 4a and 6e).

The diatexite hosts more complex microstructural relationships. The residuum plagioclase grains have grain sizes of 166 μm, generally euhedral shape with some straight grain boundaries (Figures 3b and 4d and Table 1). K-feldspar grains make up 15% of the residuum, hence are higher in abundance than that in the metatexite's residuum, and exhibit smaller grain size (122 μm). Grains occur evenly distributed with euhedral or rounded shapes among plagioclase (Table 1 and Figure 7a). Quartz is found as spherical inclusions within plagioclase grains (red arrows, Figure 4d) or as elongate quartz grain aggregates (Figure 7a). In the neosome domain, plagioclase grains are in grain clusters with curved grain boundaries, some of which have 120° triple junctions (Figures 4e and 4f). The average grain size of plagioclase in the neosome is around 175 μm and the aspect ratio is larger with 1.71 (Table 1). K-feldspar's grain size and aspect ratio are lower than plagioclase (Table 1). Hornblende's aspect ratio is clustered with an average of 1.81, the porphyroblasts are more common (33 grains) and exhibit a relatively higher aspect ratio (2.03) (Table 1). Hornblende commonly has euhedral shapes, and the average grain size is almost two times larger than that in the metatexite's residuum (Figures 3b, 4e, 4f, and 8a and Table 1). Quartz exhibits different grain shapes forming narrow linear shapes, or appear as rounded inclusions (Figures 4e, 4f, and 8a) while K-feldspar occurs

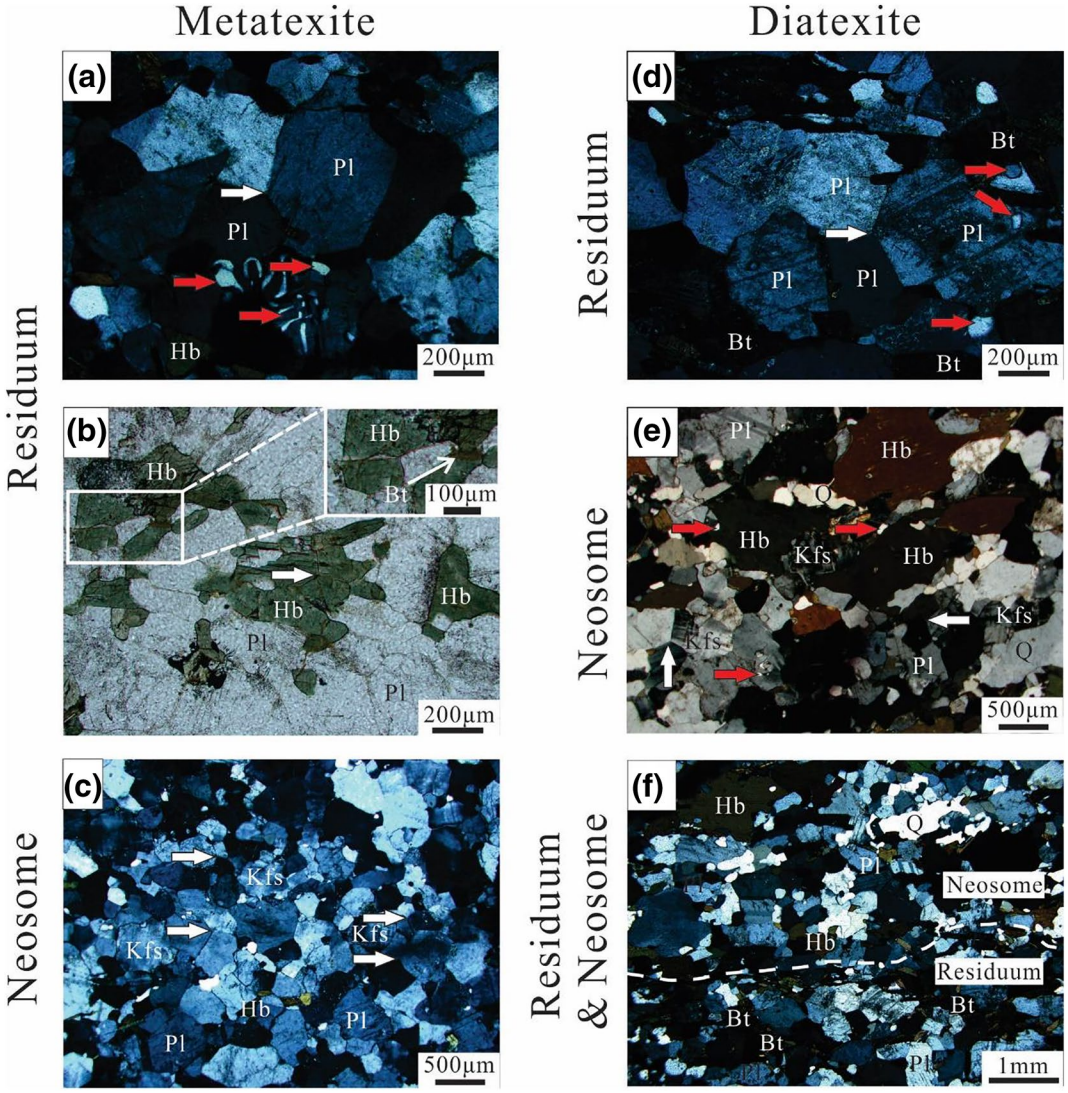

Figure 4. Photomicrographs of general microstructures of (a–c) metatexite and (d–f) diatexite. All the photos are cross-polarized light except for (b), which shows plane light; (a) residuum: equilibrium triple-junction (white arrow), K-feldspar inclusions and myrmekite textures (red arrows) between plagioclase grains, (b) residuum: anhedral hornblende grains with straight to concave grain boundaries, overprinted by ~120° triple-junction (white arrow), inset shows that biotite is surrounded by hornblende (c) neosome: mixture of even-grained plagioclase and K-feldspar with numerous equilibrium triple-junctions (white arrows), (d) residuum: plagioclase grains with straight boundaries, quartz inclusions (red arrows) and equilibrium triple junctions (white arrows), (e) neosome: 120° triple junctions exist between feldspar grains (white arrows), K-feldspar aggregates within a matrix of hornblende (coarser grained), plagioclase, quartz inclusions and myrmekite (red arrows), (f) boundary of residuum (biotite dominant) and neosome (hornblende dominant).

in multi-grain aggregates (Figure 8a). Biotite is rare in the neosome domain (Figure 8a). Additionally, it is important to note that no core-mantle structures are seen in either of the two samples. The main constituent minerals of each domain exhibit similar average long-axis orientation (Table 1).

4.3. Quantitative Crystallographic Orientation Analysis and Microstructural Data

4.3.1. Metatexite (16BT28-11)

In the residuum domain the [100] axis is parallel to lineation for plagioclase, while (010) and (001) planes are weakly parallel to foliation (Figure 5b). In misorientation angle distributions diagrams, the correlated

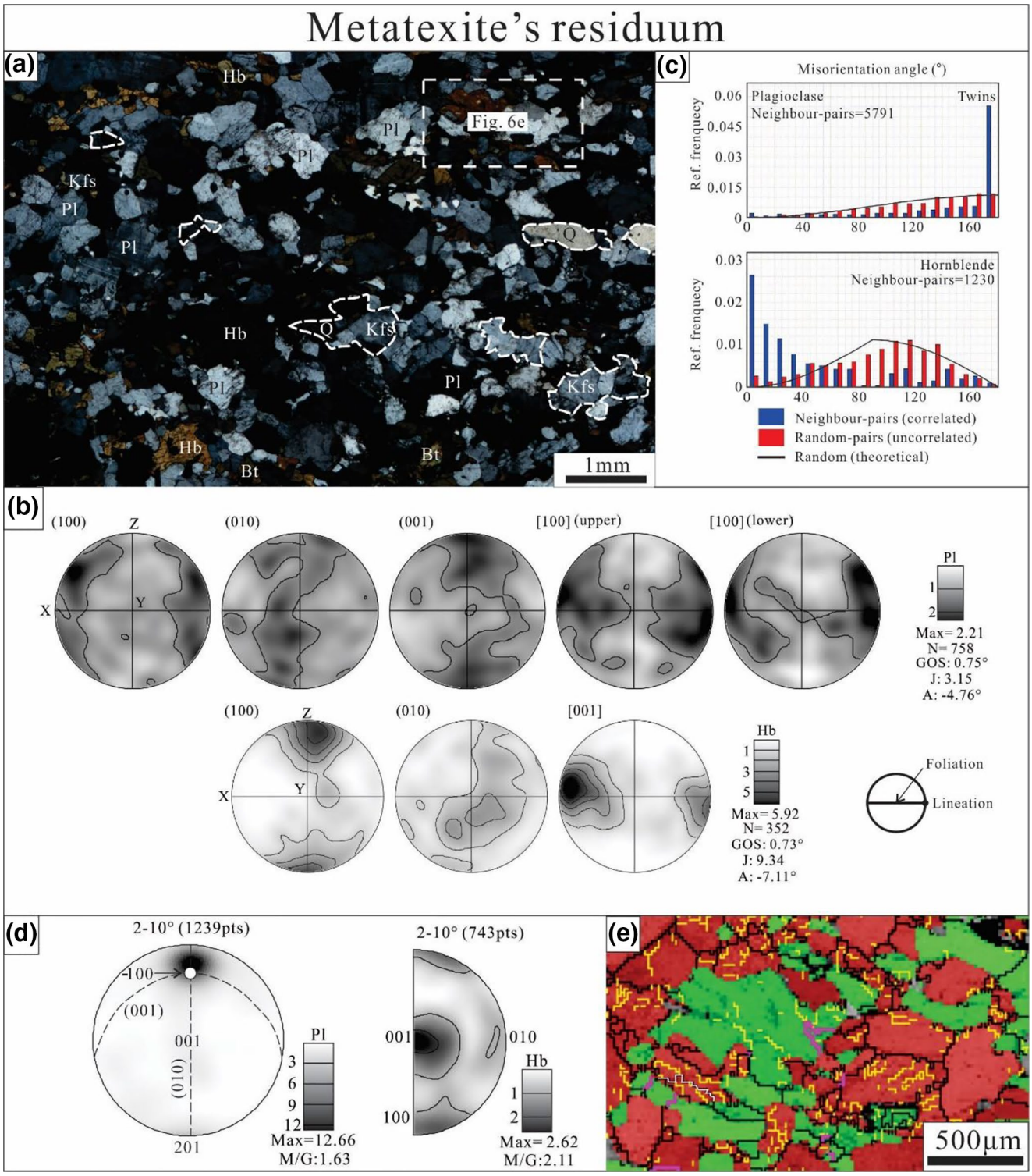

Figure 5. Orientation characteristics and EBSD map of the metatexite's residuum: (a) typical microstructure and EBSD data area in microphotograph (cross-polars); (b) crystal orientation of plagioclase and hornblende, with foliation and lineation shown; X—lineation, XY—foliation; (c) misorientation angle distributions for plagioclase and hornblende; (d) misorientation axes distribution of subgrain boundaries for plagioclase and hornblende, note the strong maxima for plagioclase around the [-100] axis; (e) representative EBSD map in residuum. White dashed line: K-feldspar and/or quartz dominant aggregate; Max: maximum density; N: number of valid mineral grains; J: J-index; A: average angle between valid grain's long axis and foliation direction (or horizontal); M/G: MXD axes/grain amounts ratio; black line: grain boundary (>10°); yellow and purple lines signify subgrain boundaries between 2–5° and 5–10°, respectively; white line: twin boundary. Gray areas are not indexed.

data for plagioclase has a relatively high frequency for the low misorientation angles (0–50°) while the uncorrelated data shows a distribution mimicking the theoretical curve (Figure 5c). This is consistent with the fact that plagioclase exhibits abundant subgrain boundaries in EBSD phase and grain maps (Figure 5e) and clear intracrystalline lattice bending within individual grains (Figure 9a). Plagioclase misorientation axes are clustered around the [-100] direction, the intersecting point between (010) and (100) planes (Figure 5d). For hornblende, the (100) plane is parallel to the foliation and the [001] directions are sub-parallel to the lineation (Figure 5b). Here, the misorientation angle distribution shows high than random frequencies in the low-angle area (0–50°, especially for 0–10°) for correlated data, while uncorrelated data demonstrates a weak bimodal distribution deviating from expected frequencies associated with a random orientation distribution (Figure 5c). The misorientation axis distribution pattern is consistent with hornblende grains frequently exhibiting subgrain boundaries and preserving some intracrystalline deformation from grain center to rim (Figures 5e and 9a). Misorientation axes distribution shows clustering around [001], although some axes are centered around the [100] direction (Figure 5d). Both plagioclase and hornblende have similar GOS values and average long axes angles to horizontal direction (0.75 and −4.76 for plagioclase, 0.73 and −7.11 for hornblende), and the angles are coincide with the [100] (plagioclase) and [001] (hornblende) directions in pole figures. However, hornblende has significantly larger MXD axes/grain amount ratio and J-index than plagioclase (Table 1 and Figure 5b).

Plagioclase grains in the neosome show similar crystallographic orientation patterns as the residuum (shown in pole figures and MXD figures) although the (001) plane is closer to foliation-parallel (Figures 6b and 6d). The misorientation angle distributions diagram for random-pairs reveals a weak bimodal distribution and a high frequency of neighbor-pairs for medium angles (40–50° area; Figure 6c). The misorientation axes distribution tends to be concentrated between [-100] and [201] (Figures 6b–6d). Plane (010) in K-feldspar aligns with foliation and axis [100] with lineation (Figure 6b). In misorientation angle distributions diagram the mineral has a weak bimodal distribution (random-pairs), and relatively high frequency for 0–50° for both neighbor- and random-pairs (including 0–10° in neighbor-pairs; Figure 6c). For the misorientation axes, K-feldspar are around [001] direction mainly and [100] as secondary maximum, MXD axes/grain amount ratio in plagioclase is higher than that in K-feldspar (Table 1 and Figure 6d). Feldspars (plagioclase and K-feldspar) have similar GOS, J-index and angle from horizontal to mineral long axis (Table 1 and Figure 6b). Both feldspars show subgrain boundaries in EBSD phase and grain maps consistent with noted misorientation angle distribution patterns (Figure 6e) with frequent subgrain boundaries (2–5° misorientation) within individual grains (Figure 9a). In the neosome, the plagioclase is similar to the residuum. The plagioclase's long shape axis and the [100] direction largely coincide; however, this is not the case for K-feldspar (Figure 6b). While K-feldspar dominates the neosome domain (much lower Pl/Kfs ratio than residuum; Table 1 and Figure 6a), its 2–10° misorientation angle frequency is lower than that for plagioclase (Figure 6d). Maps show that only some K-feldspar grains exhibit strong internal crystal lattice bending (Figure 9a).

4.3.2. Diatexite (16BT14-3)

Plagioclase in the diatexite's residuum domain exhibits (001) plane sub-parallel to foliation, most [100] directions are parallel to lineation (Figure 7b). The misorientation angle distributions are similar to that seen for the neosome in the metatexite, however, there is higher frequency in both neighbor- and random-pairs in several ranges (0–10°, 30–90°, 140–160°) (Figure 7c). The intracrystalline deformation of plagioclase grains is obviously lower than the metatexite's domains (fewer subgrain boundaries, lower M/G values and misorientation changes; Figures 7d and 9b). K-feldspar's CPO is non-random with plane (001) parallel to foliation (Figure 7b). The K-feldspar misorientation angle distributions diagram shows high frequency for 0–20°, 40–60° and 80–90° ranges in random-pairs data and high frequency in 0–40°, 70–110°, and 130–150° ranges for neighbor-pairs data (Figure 7c). 2–10° misorientation axes show a dominance of the [001] axis (Figure 7d). The MXD axes/grain amount ratio for K-feldspar is larger than for plagioclase (Figure 7d). The feldspar grains have similar GOS, long axis angles to the main foliation (15.61° and 18.02°) and higher J-indices (13.4 and 10.7) (Table 1 and Figure 7b). In the neosome, the plagioclase CPO is characterized by [100] axis parallel to lineation, while the (010) and (001) planes are weakly parallel to foliation; hence the CPO pattern is similar to that of the residuum in the metatexite (Figure 8b). In the misorientation angle distributions diagram, plagioclase's neighbor-pairs data has higher frequency than theoretical at low-to

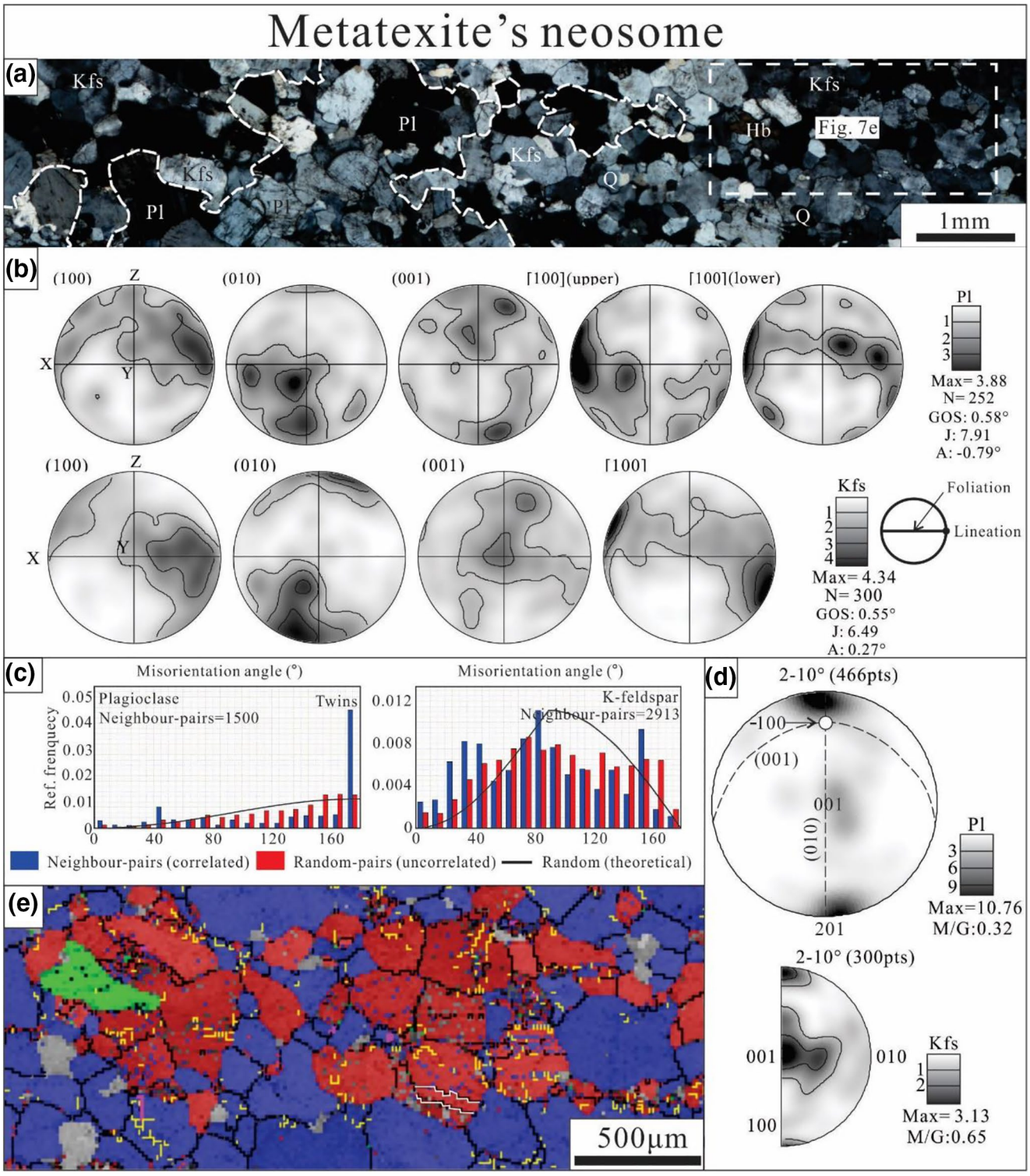

Figure 6. Orientation characteristics and EBSD map of the metatexite's neosome: (a) typical microstructure and EBSD data area in microphotograph (cross-polars); (b) crystal orientation of plagioclase and K-feldspar, with foliation and lineation shown; X—lineation, XY—foliation; (c) misorientation angle distributions for plagioclase and K-feldspar; (d) misorientation axes distribution for plagioclase and K-feldspar; (e) representative EBSD map in leucosome. White dashed line: plagioclase dominant aggregates (sometimes with hornblende). Blue: K-feldspar; Red: plagioclase; Green: hornblende; other parameters and legends are same as shown in Figure 5.

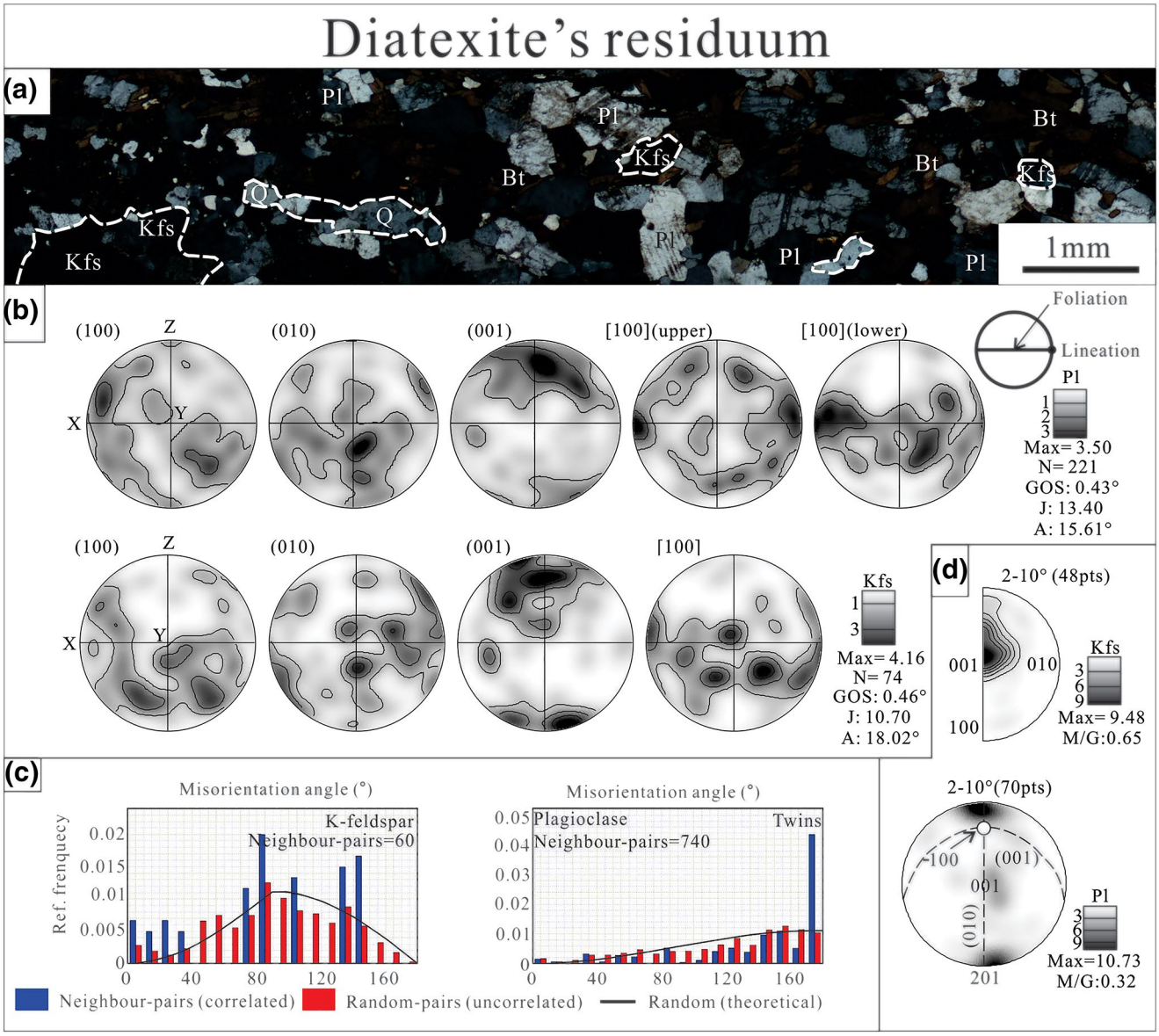

Figure 7. Orientation characteristics of diatexite's residuum: (a) typical microstructure and EBSD data area in microphotograph (cross-polars); (b) crystal orientation of plagioclase and K-feldspar, with foliation and lineation shown; X—lineation, XY—foliation;; (c) misorientation angle distributions for plagioclase and K-feldspar; (d) misorientation axes distribution for plagioclase and K-feldspar. All the parameters and legends are the same as Figure 5 shows.

medium angles (0–60°) (Figure 8c). The misorientation axes distribution is clustered between [-100] and [201] direction but the axis number is much less than the metatexite's residuum (Figure 8d). For individual grains, not only much fewer subgrain boundaries exist, but their misorientation angle is lower (mostly lower than 2°; Figure 9b). K-feldspar in the neosome has a weak CPO similar to that of the metatexite's neosome. The misorientation angle distribution demonstrates high frequency in 0–80° (neighbor-pairs) range, 0–10° angles show a higher frequency than that expected for a random distribution (shown as the black line in Figure 8c) and are more pronounced than that for plagioclase. The misorientation axes distribution pattern is almost the same as for the metatexite's neosome domain, while absolute number of misorientation axes is only about half (176 pts) (Figures 8b–8d). Hornblende's (100) and (010) planes are coupled as seen on a pole figure similar to the metatexitie's residuum with direction [001] parallel to lineation and the alignment of [001] being more pronounced than that of (010) (Figure 8b). Misorientation angle distribution neighbor-pair data has a higher frequency than the theoretical for angles of 0–70°. Angle area of 0–10° is

much higher than theoretical but are not as pronounced as that in the metatexite. Misorientation axes are randomly distributed and the amount is less than half of the metatexite's residuum (338 pts) (Figures 8b–8d). Internal deformation of hornblende shows that there is significant crystal bending close to grain edges while the center of grains reveal little intracrystalline deformations. (Figure 9b). In addition, for biotite in the residuum domain, the (100) plane is close to the Y direction, (010) plane is subparallel to the YZ plane, [001] axes are parallel to the Z direction (Figure S1).

Plagioclase, K-feldspar and hornblende have similar angles between their long shape axis and the foliation (Figure 8b) and all exhibit within the neosome a misorientation angle distribution close to that expected from a random orientation distribution (Figure 8c). MXD axes/grain amount ratio and J-index are increasing from plagioclase, to K-feldspar to hornblende. GOS for K-feldspar is higher than that for plagioclase and hornblende (Table 1 and Figures 8b and 8d).

5. Discussion

5.1. Identification of Phases During Migmatization

Felsic minerals such as quartz, plagioclase and potassium feldspar are usually considered as evidence for previous melt in the anatexites (Hasalová et al., 2008; Lee et al., 2017; Sawyer, 1999, 2001). Accordingly, we suggest that the neosome domains in the two migmatites represent areas of high melt presence during the migmatization event (Sawyer & Brown, 2008). Field relationships shows that the diatexite outcrops have more obvious anatectic flowing textures than the metatexite outcrops (Figure 2).

The estimated amount of neosome in the diatexite outcrops (not including later injected veins) is markedly higher than that in the metatexite outcrops, supported by both hand specimen and microscale observation of the two studied samples (Figure 3 and Table 1). In the residuum domain, both K-feldspar and quartz grains in the samples are aggregated (Figures 5a and 7a) or in the case of quartz, also form inclusions or linear shapes (Figures 4a, 4d, and 4f). We suggest that during the migmatization event a small amount of melt may have existed within the residuum where K-feldspar and quartz represent the in-situ melt. The two migmatites' selected neosome domains have different modal mineral contents (Table 1). K-feldspar in the metatexite (54.5%) and plagioclase in the diatexite (29.7%) are the main felsic minerals in the neosome domain. Quartz in these domains is not so much (4.4% in metatexite and 18.9% in diatexite) exhibiting either a rounded or linear shape in (more obvious in the diatexite; Figures 4e, 4f, 6a, and 8a). K-feldspar and plagioclase show less pronounced crystal plastic deformation features (such as low 2–10° misorientation axes/grain amount ratio, GOS value and abundance of internal deformation; Table 1 and Figures 6d, 8d, and 9) than in residuum domains. In the neosome domain, K-feldspar in the metatexite exhibits less internal deformation than plagioclase, and plagioclase in the diatexite is less deformed within individual grains than K-feldspar (Table 1 and Figures 6d, 8d, and 9). We suggest that these weakly deformed minerals were initially melted during the peak of the migmatization event and recrystallized from the melt later (Figures 6a and 8a; Pakrash et al., 2018), rounded grains in the neosome might be the new-generated melt before the last final melt frozen (Figures 4c, 4e, and 6e). During syn-melt conditions in the neosome, we consider there was a mixture of solid phases and melt. The solid phases are plagioclase in the metatexite and hornblende and K-feldspar in the diatexite. The chemistry of the melt phase is dominated by K-feldspar in the metatexite, and plagioclase in the diatexite. These minerals experience deformation both prior to and after the partial melting condition, so that their deformation characteristics are stronger than those developed at the post-melt condition only (Table 1 and Figure 9). Therefore, these minerals are introduced as a reference to divide solid and liquid phase in the syn-melt condition. Accordingly, considering K-feldspar and quartz as the melt phases in the metatexite's neosome, and plagioclase and quartz in the diatexite's neosome, the melted areas in the two samples are ~25% in the metatexite and ~50% in the diatexite (Table 1).

The two migmatites exhibit features in the field and under the microscope that are markedly influenced by melt, this separates the period before the melt presence and after the melting period. Deformation characteristics in different rocks allow us to identify which characteristics are typical for the rock in the three main periods of its evolution, namely pre-, syn- and post-melt. Due to the neosome domains in the two migmatites revealing different deformation degrees in different minerals, we infer that neosome, minerals with weaker deformation characteristics belong to liquid phase during the syn-melt condition, and the post-melt

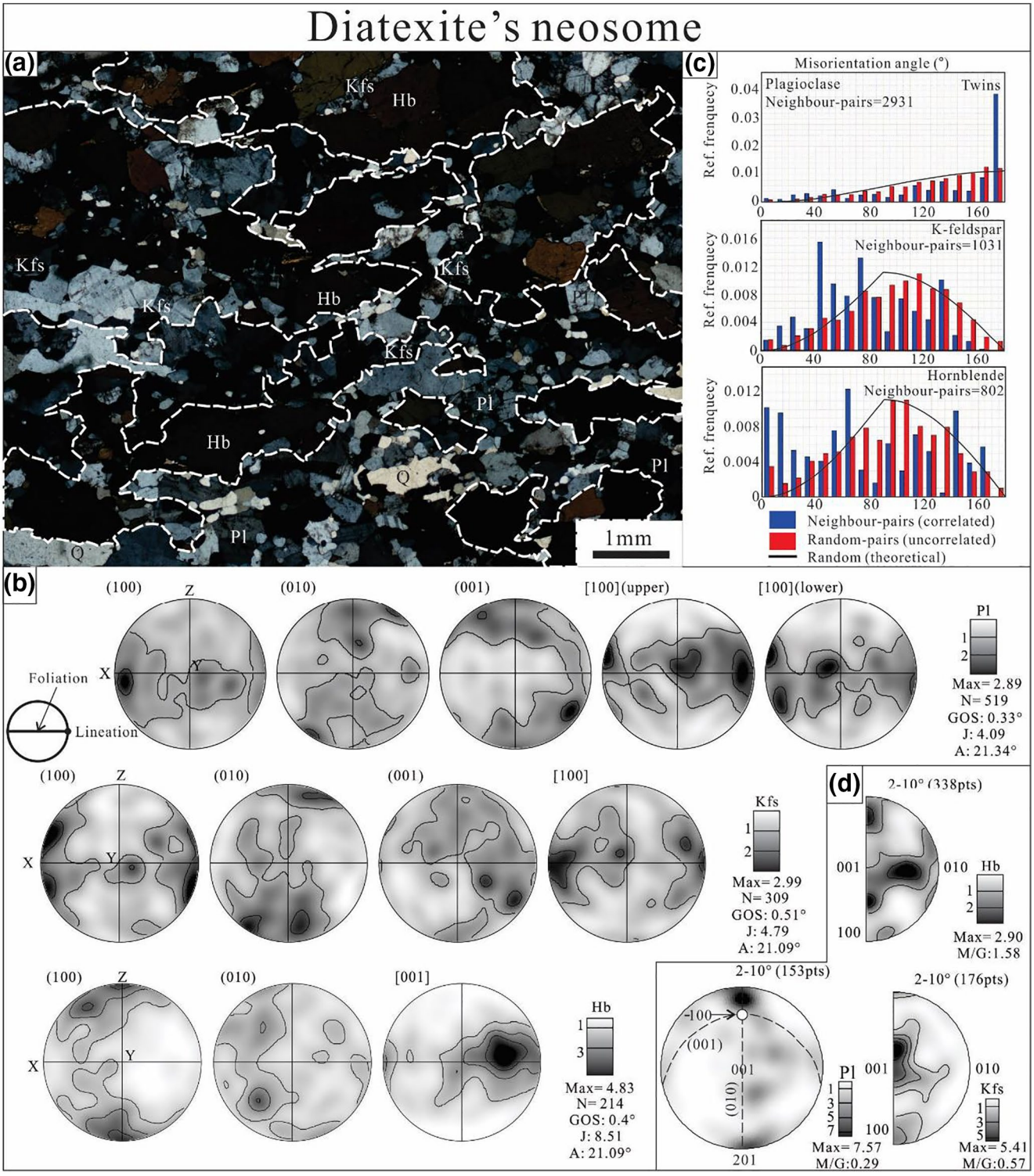

Figure 8. Orientation characteristics of diatexite's neosome: (a) typical microstructure and EBSD data area in microphotograph (cross-polars); (b) crystal orientation of plagioclase, K-feldspar and hornblende, with foliation and lineation shown; X—lineation, XY—foliation; (c) misorientation angle distributions for plagioclase, K-feldspar and hornblende; (d) misorientation axes distribution for plagioclase, K-feldspar and hornblende. White dashed line: represent plagioclase and hornblende dominant aggregates. All the parameters and legends are the same as Figure 5 shows.

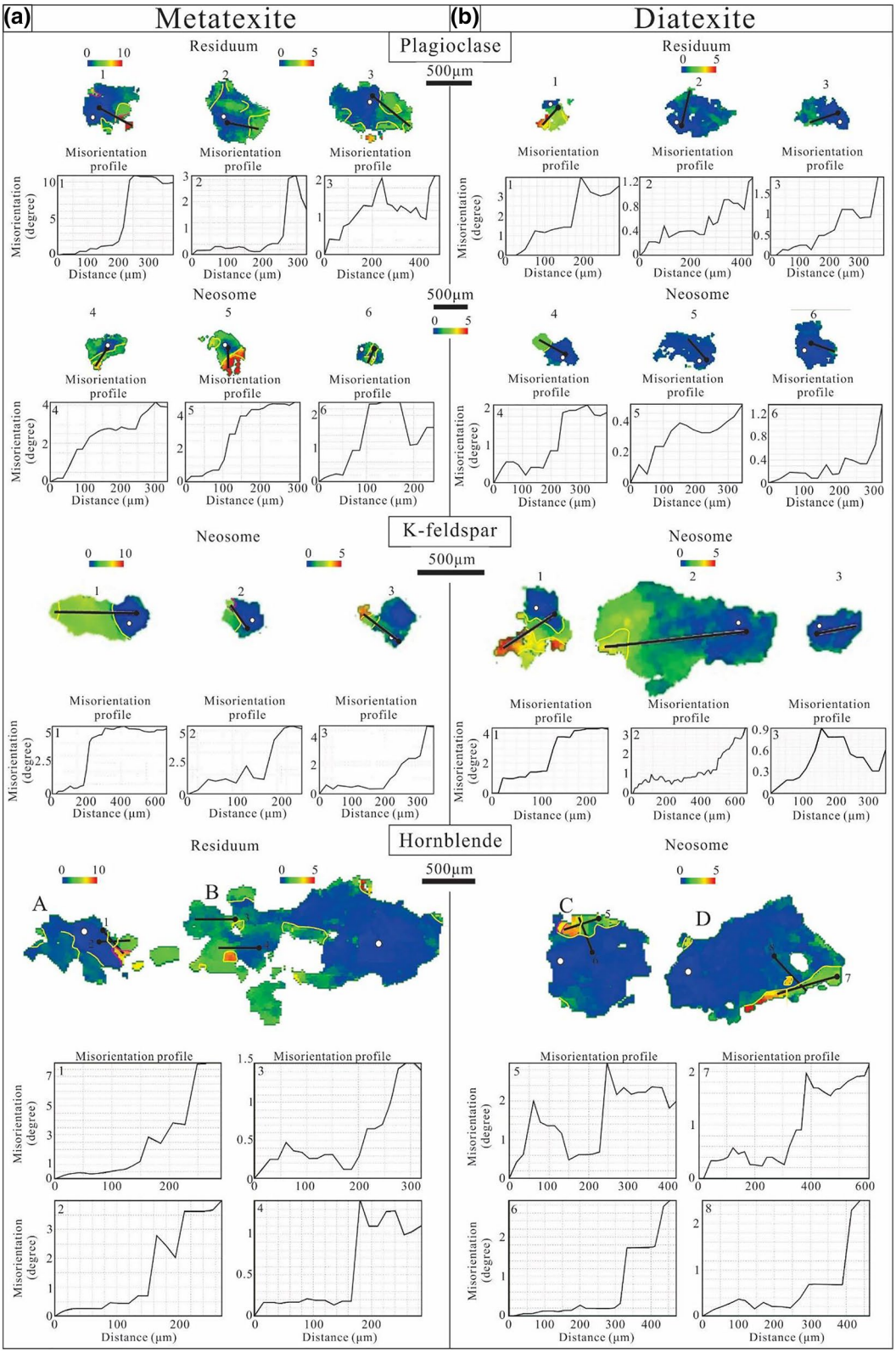

Figure 9. Typical intracrystalline deformation features of plagioclase, K-feldspar and hornblende grains in the metatexite (a) and diatexite (b). Orientation changes are shown in degrees relative to a reference orientation (marked as white spot); the starting point for misorientation profiles are shown (0 μm) is marked as black spot; yellow and purple lines represent 2–5° and 5–10° subgrain boundaries.

deformation is weaker than that during the pre-melt condition. Based on this discovery, the dominant deformation progress in residuum took place in the pre-melt condition. In summary, the residuum represents mainly the pre-melt situation, especially for the diatexite, as we suggest that based on field relationships and the composition of the observed neosome is largely externally derived, that is, not derived directly by partial melting of the rock in which it resides. In other words, at syn-melt conditions, only minor partial melting occurred in-situ in the residuum while the majority of the neosome domain is derived externally, that is, originating from rock at distance to the actual rock investigated. For the diatexite, partial melting was more pronounced. The post-melt situation is represented by both residuum and neosome's "frozen" microstructure (Table 2 and Figure 10). In the following section, we discuss the detailed microstructural evolution in the pre- (residuum only), syn- (mostly neosome) and post-melt (mostly neosome) conditions.

5.2. Deformation Conditions and Mechanisms of Migmatite's Residuum and Neosome

5.2.1. Pre-Melt Condition and Deformation Mechanisms

In the metatexite, plagioclase has equant grains (Figure 5a), and frequent subgrain boundaries and their axes (or misorientation axes distributions) represents the existence of (001) [100] CPO, pointing to the importance of dislocation creep and thus power-law creep behavior (Figures 5d, 5e, and 9a and Table 2; Ji et al., 2004; Kruse et al., 2001; Marshall & McLaren, 1977). For hornblende grains (Figures 4b, 5a, and 5e) subgrain misorientation axes are clustered near the [001] direction. (100) [001] is inferred as the main slip system for the hornblende in this domain (Figure 5b; Díaz Aspiroz et al., 2007; Getsinger & Hirth, 2014). In addition, low-angle neighbor-pairs data (0–10°) are high in frequency, confirming significant intracrystalline deformation in the hornblende (Figures 5c, 5e, and 9a). Accordingly, we believe that dislocation creep plays an essential role in the hornblende deformation during the pre-melt condition. This absence of core-mantle textures and numerous curved grain boundaries observed in hornblende (Figures 4a and 5a) is consistent with high temperature deformation where GBM plays a significant role (Table 2; Passchier & Trouw, 2005; Rosenberg & Stünitz, 2003). K-feldspar has a weaker CPO (Figure 7b) but higher GOS and M/D value than plagioclase (Table 1 and Figure 7d), this supports our interpretation that this mineral was mostly deformed during the pre-melt condition. Misorientation axis distribution has similar distribution to K-feldspar in other domains, which also indicate dislocation creep (Figure 7d; Ishii et al., 2007). However, some component of crystal plastic deformation is shown by the [001] direction being closer to Y axis in the pole figure and higher MXD axes/grain amount ratio suggest that lattice orientation was not so accordant as in other domains (Bestmann & Prior, 2003; Table 1 and Figure 7b).

Plagioclase in the diatexite has a similar curved grain shape as in the metatexite (Figures 4d, 4f, and 7a), but exhibits a more prominent CPO, suggesting dominance of the (001) [100] slip system. The field outcrops show that the diatexite are more influenced by ductile shearing at higher temperatures (Figures 2d–2f; Cai et al., 2014; Cai, Liu, Liu, Liu, et al., 2013; Cai, Liu, Liu, Shi, et al., 2013), consequently, the CPO and J-index are much stronger (Table 1 and Figure 7b). The simultaneous lower frequency of subgrain boundaries suggests that GBM in plagioclase was more pronounced leading to a decrease in the number of subgrains (Figure 4d and Table 2; Urai et al., 1986; Passchier & Trouw, 2005).

5.2.2. Syn-Melt Condition and Deformation Mechanisms

Microstructural observations of the residuum in the two migmatites shows they have experienced partial melting, which is characterized by oriented linear shaped quartz grains and/or K-feldspar aggregates (Figures 4a, 4d, 5a, and 7a). The diatexite's residuum has a larger melt mineral content than the metatexite's (Table 1). Photomicrographs and EBSD maps of the metatexites' neosome show that it is strongly aligned to the foliation both macro- (Figures 3a–3c) and microscopically (Figures 3a and 5a), which suggests that melt migration was syntectonic (Sawyer, 2001). Plagioclase in the neosome has similar deformation characteristics to that in the residuum (Figures 6d, 6e, and 9a), and small hornblende grains are present in the neosome's plagioclase aggregate (Figures 4c, 6a, and 6e). We suggest that these areas originate from the residuum and form remnant "islands" within the melt injection dominated neosome. K-feldspar has weaker deformation characteristics than plagioclase, therefore we suggest that it represents a significant part of the melt that injected the residuum during melt present deformation (Table 2 and Figure 10).

Table 2
Overall Deformation and Rheological Characteristics of Two Migmatites in Different Melting Periods

		Pre-melt	Syn-melt		Post-melt
Rock type	Characteristics	Residuum	Residuum	Neosome (with crystalline material in melt)	Residuum and neosome
Metatexite	General microstructures	Both plagioclase and hornblende have numerous subgrain boundaries. Plagioclase has euhedral grains while hornblende has anhedral grains.	Similar to the pre-melt condition.	Plagioclase (with minor hornblende) has similar characteristic as that in residuum, and surrounded by K-rich melt.	K-feldspar grains in neosome were equant, and the grain shape was similar to plagioclase in both domains. Some additional subgrain boundaries, and straight grain boundaries with 120° triple junctions were generated in feldspars in two domains, some hornblende grains in residuum were accompanied by biotite.
	Deformation mechanism	Minerals experienced dominant dislocation creep (GBM in plagioclase) with some subgrain formation in high temperature.	Dislocation creep was stopped, K-feldspar and quartz were in melt status.	Plagioclase should be originally from residuum and keeps similar microstructural characteristics.	Dislocation creep (GBM) and subsequent annealing process were added in two feldspars in both domains.
	Rheological distribution	Power-law behavior dominant.	Largely rigid with minor melt flow.	Rheology dominated by melt (Newtonian).	Power-law, weaker than the pre-melt condition, strain localization might be existed in restricted neosome.
Diatexite	General microstructures	Plagioclase grains are equant and curved in high temperature, with much fewer subgrain boundaries.	Similar to that in the metatexite, the melting degree was higher.	K-feldspar and hornblendes were crystallized in this period, hornblende had larger grain size than in the metatexite, they are surrounded by dominant melt. These solid phases might preserve minor earlier deformation features.	In residuum, feldspars have lower grain size and fewer subgrain boundaries than neosome, accompanied with straight grain boundaries and 120° triple junctions. In neosome, feldspars experienced similar process like in the metatexite's neosome and the grain shapes are more curved, K-feldspar has stronger deformation characteristics than plagioclase, and subgrain boundaries in hornblende are mostly existed in rim area.
	Deformation mechanism	Main dislocation creep (GBM), which might be erased by later partial melting process in high temperature.	Very little deformation with melt inhabitation.	Little deformation in this period, hornblende was influenced by rigid body rotation with dissolution-precipitation creep, hornblende result of peritectic reaction.	Hornblende experienced minor deformation fracturing and healing of fractures, K-feldspar exhibit irregular grain boundaries, deformation by GBM; less pronounced in plagioclase.
	Rheological distribution	Power-law behavior dominant.	Softer than the metatexite's residuum but harder than neosome, the restricted melt flow is stronger than matatexite's residuum.	Similar to the metatexite, with higher strain due to dominant melt flowing (Newtonian) with low viscosity.	Power-law, rheologically weaker than the pre-melt condition, but stronger than the metatexite, strain localization might exist in restricted residuum.

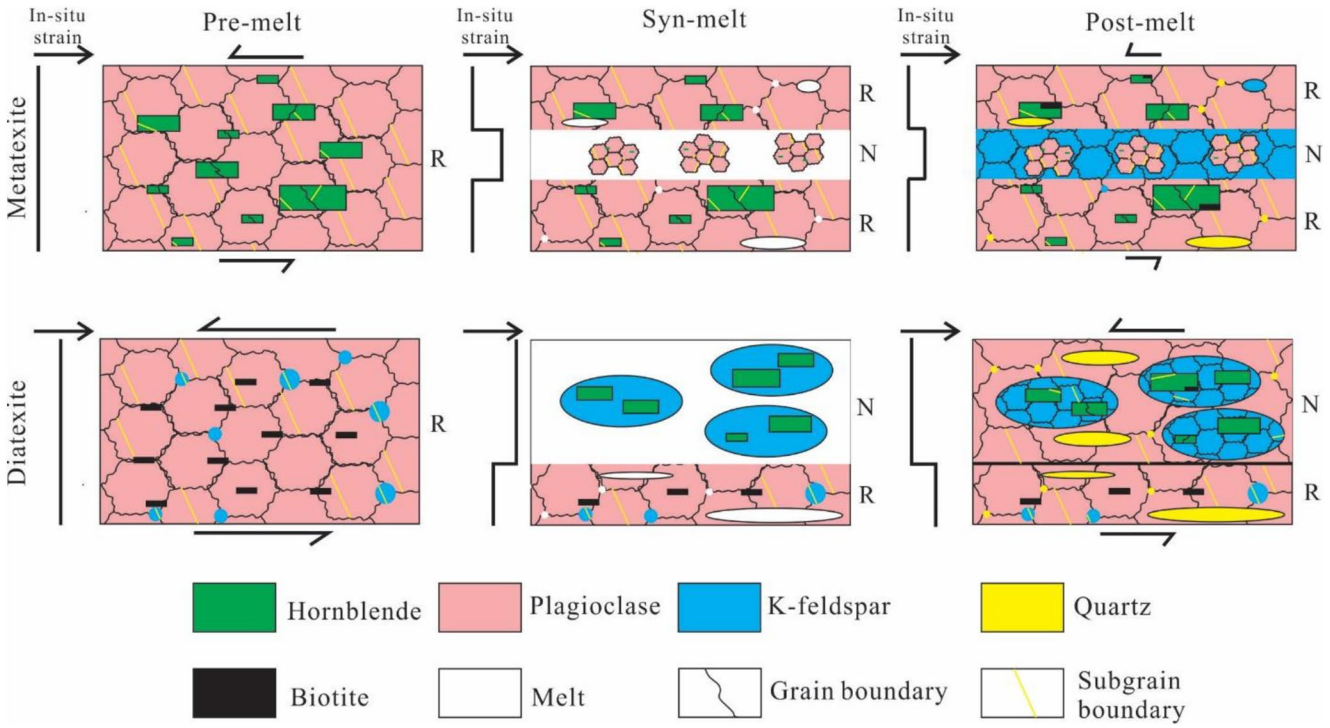

Figure 10. Models of migmatites' deformational evolution procedures in pre-, syn-, and post-melt stages in ductile shearing environment (not to scale). The arrow represents strain increasing and the fold line represent relative strain degree in different domains. R, residuum; N, neosome.

In the diatexite's neosome, plagioclase is randomly and irregularly distributed (Figure 8a), suggesting that it crystallized out at the veining stages of migmatization (Sawyer, 2001; Stuart et al., 2018). The signatures of internal deformation (MXD axes/grain amount ratio, GOS, J-index in Table 1 and intracrystalline deformation features in Figure 9b) are more pronounced in hornblende and K-feldspar suggest stronger deformation than plagioclase. We infer that the hornblende and K-feldspar form clear phenocrysts in the neosome; the hornblende has almost two times the average grain size than that in the metatexite's residuum (Table 1 and Figure 8a). It also exhibits a euhedral shape with felsic inclusions and very little recrystallization features (Figures 4e, 8a, and 9b). Such characteristics can be attributed to a peritectic reaction at granulite facies conditions (Busch et al., 1974; Hu et al., 2016; Weinberg & Hasalová, 2015). Hornblende is well oriented with high aspect ratio, and the orientation tendency (long-axis angle) is similar to [001] direction (i.e., the coherent SPO and CPO; Table 1 and Figures 8a and 8b), accompanied with near random misorientation angle distributions (random-pair, similar distribution to theoretical) and strain-free internal structures of hornblende grains (Figures 8c and 9b). These features are consistent with rigid body rotation with dissolution-precipitation creep (Berger & Stünitz, 1996; Díaz Aspiroz et al., 2007; Imon et al., 2004). Although the gneissosity of the diatexite is not as obvious as in the metatexite, the linear- to rectangular shaped quartz shows a distinct parallel-to-foliation tendency (Figures 4e, 4f, and 8a) suggesting syn-tectonic migmatization (Figure 10). Rheologically, for both the metatexite and diatexite, the flow properties of the bulk rock would have been dominated by the properties of the melt, suggesting Newtonian flow characterized by not only a marked difference in the strain rate to differential stress relationship but also lower overall viscosities than those at pre- and post- melt conditions (Table 2; e.g., Champallier et al., 2008).

5.2.3. Post-Melt Condition and Deformation Mechanisms

For the metatexite there is very little evidence, both in the outcrops and at the thin section scale, of the retrogression due to later exhumation; only in areas where hornblende grains are replaced by biotite in the residuum (Figures 4b and 5a and Table 2). This replacement, however, could be due to H_2O-rich fluids expelled by the crystallizing melt facilitating the growth of a high temperature biotite at near peak metamorphic conditions (Kriegsman, 2001; Speer, 1987). Hence, post-melt features are interpreted to be representative of

lower crustal processes. In the metatexite's neosome, K-feldspar exhibits some subgrains that relate to the activation of a high-temperature slip system (Figures 6d and 6e). The subgrain boundaries in the K-feldspar imply that dislocation creep took over as the dominant deformation mechanism after melt frozen, however, the low frequency of subgrain boundaries and lower GOS value in K-feldspar in the neosome suggest that the finite strain was minor (Tables 1 and 2 and Figures 6d and 6e). K-feldspar in this domain exhibits activation of the (010) [100] slip system (Figure 6b; Martelat et al., 1999). Both residuum and neosome's feldspars frequently exhibit 120° triple junctions (Figures 4c, 5a, and 6a), which may be due to annealing (static recrystallization) process after melt crystallized (Dallain et al., 1999; Flinn, 1969; Smith et al., 2015).

It is striking that within the residuum of the diatexite, an extremely high J-index is observed for both plagioclase and K-feldspar (Table 1 and Figure 7b). This may suggest that the finer grained plagioclase in the residuum hosted most of the deformation not only during pre- but also post-migmatization (Figure 10). This is also the case for the fine-grained K-feldspar in the residuum, its high J-index is likely also related to both pre- and post-migmatization deformation. In the diatexite's neosome, the crystallized plagioclase exhibits only locally microstructural features typical for high temperature GBM recrystallization, that is, irregular boundaries and crystal lattice bending within grains (Figures 8a and 9 and Table 2). In addition, the CPO is weaker and subgrain boundary frequency is lower than in other domains (Figures 8b and 8d). The less pronounced signature of solid-state deformation for plagioclase within the neosome implies that deformation during the post-melt condition was weaker than during the pre-melt condition. K-feldspar shows irregular boundaries suggesting GBM (Figure 8a and Table 2). The CPO ((010) [100]) and misorientation axes distributions are similar to that in the metatexite's neosome (Figures 6b and 6d), suggesting some influence of dislocation creep. For individual grains of hornblende, both (100) [001] and (010) [001] were activated with random MXD (Figures 8b and 8d; Díaz Aspiroz et al., 2007; Getsinger & Hirth, 2014). Therefore the “subgrain boundaries” could be considered as healed cracks in the post-melt condition (Danner et al., 2019), they are fewer and distributed around the grains' rims, most core areas of the hornblende grains are strain-free, suggesting that the later stage deformation took place at the rim of the grains (Figure 9b). According to the information mentioned above, we infer that the described deformation features of the K-feldspar and hornblende were produced dominantly at post-melt conditions (Figure 10). The two migmatites have similar feldspar grain size (Table 1), and there is no evidence for grain size reduction post crystallization (e.g., core-mantle or mylonitic texture). Consequently, there is no evidence for a tectono-metamorphic signature within the areas of former melt dominance post melt crystallization (Elías-Herrera & Ortega-Gutiérrez, 2002; Passchier, 1984). Thus, we infer no significant post crystallization deformation occurred in the solidified neosome.

During post-migmatization, in the residuum deformation was dominated by dislocation creep with possible strain localization into this domain (Tables 1 and 2 and Figure 10). This interpretation is supported by the narrow residuum domain having, relative to the neosome, a smaller grain size, stronger CPO and higher aspect ratio, GOS value, J-index and aligned biotite, which all indicate higher strain (or strain rate) (Table 1 and Figures 6b and 7b; Hansen et al., 2014; Mainprice et al., 2014; Morales & Tommasi, 2011; Rybacki & Dresen, 2004; Warren & Hirth, 2006).

The similar aspect ratios of plagioclase in the two domains of the diatexite may point to effect of a late annealing process (Table 2).

5.3. Implications for Lower Crustal Rheology

Based on the previous discussion, the following rheological evolution can be concluded (Table 2, Figure 10). During the pre-melt condition, power-law (i.e., dislocation creep) dominates the residuum of the two migmatites. At syn-melt condition Newtonian melt flow dominated the rheology of the both rocks as both exhibit a melt fraction significantly above 50% melt (by calculating total melted minerals in Table 1; Burg & Vigneresse, 2002; Champallier et al., 2008; Lejeune & Richet, 1995; Rosenberg & Handy, 2005), with viscosities significantly lower than at the time of the other two evolutionary stages. During the post-melt condition when trapped melt crystallized in situ, grain sizes are larger in the neosome and low strain is accommodated by dislocation creep with a power-law stress–strain rate relationship. However, post-migmatization deformation features are subtle even in the residuum, hence we interpret that the rocks experienced only

minor deformation, deeming it relatively strong. The in-situ migmatites are either middle or lower crustal rocks, depending if the crust is overthickened.

6. Predicted Seismic Signals of the Lower Crust during Pre-, Syn- and Post-migmatization

6.1. Method

To calculate the seismic properties, we used the MTEX and MSAT toolbox based on Matlab utilizing the orientation data from EBSD analysis (Lee et al., 2017; Mainprice et al, 2011, 2014; Walker & Wookey, 2012). Elastic moduli of related minerals at ambient conditions were used (Aleksandrov & Ryzhova, 1961; Aleksandrov et al., 1974; McSkimin et al., 1965), while the melt's elastic moduli are based on Rivers and Carmichael (1987). Since we consider a polymineralic assemblage, we used the Voigt-Reuss-Hill average tensor method (Hill, 1952; Mainprice, 1990). We calculate seismic velocities for the pre-, syn- and post-melt conditions taking data from different parts of the rock into account. Data from the residuum domain is used to simulate the pre-melt conditions. For the syn-melt conditions, data from the residuum without partial melt and the minerals interpreted to have been present as a solid within the melt (now neosome) are used. Considering the melt in neosome plays a main role in this period, we simulated 60% melt in the metatexite's neosome and 50% melt in diatexite's neosome, which are similar to the percentage of melted minerals in individual domains (Table 1). The minor partial melting process in residuum domains were not considered in this case study. The melt simulation process was calculated using the MSAT toolbox based on Lee et al. (2017) and Walker and Wookey (2012). The shape of melt inclusions was modeled to be oblate with an aspect ratio is 10:10:1 according to the dominantly oblate shape of the neosome observed in our field example where the neosome forms part of the foliation (Figure 3). For the post-melt conditions data from the whole rock is utilized (see Figure 11 for detail). The volume fractions of minerals in the different conditions were based on EBSD data shown in Table 1. The pre-melt condition is best recorded in the non-melted minerals in the residuum, namely plagioclase and hornblende in the metatexite and plagioclase, K-feldspar and biotite in diatexite (Figure 11). The syn-melt condition can be derived from minerals from part of residuum mentioned above, identified as solid phase in the neosome (plagioclase and hornblende in the metatexite, K-feldspar and hornblende in diatexite) and melt (the volume is same as the minerals identified as melt in neosome, K-feldspar and quartz in the metatexite, plagioclase and quartz in diatexite) (Figure 11). The post-melt condition is exemplified by the characteristics of the whole rock (see Figure 11). Rock density in different domains was calculated based on the volume fractions of minerals (minerals lower than 1% in each domain were not considered, see Table 1). The elastic constants of samples in different situations are provided in the supporting information (Table S1). The orientation of the seismic figures' is the same as the pole figures, foliation-parallel to XY plane, lineation parallel to X direction.

6.2. Seismic Calculations - General Trends

In the metatexite, the magnitude of P-wave velocities and most seismic anisotropies are similar but higher for the pre-melt than post-melt conditions, while shear wave seismic anisotropies in melting conditions are the highest, shear wave velocity and Vp/Vs ratios are similar in both pre- and post-melt conditions (Table 3 and Figure 11). For the syn-melt condition, seismic velocities are lower, seismic anisotropies are far greater than observed pre- and post-melt. Syn-melt maximum Vp/Vs ratios are higher than observed pre- and post-melt, while minimum Vp/Vs ratios are closer to those conditions (Table 3). The seismic figures for the pre-melt condition shows the maximum P-wave velocity is sub-parallel to the X axis and minimum zone is sub-parallel to YZ plane, maximum S-wave anisotropies are concentrated on XY plane (i.e., foliation plane), Vs_1 maximum zones have a similar distribution while Vs_2 maximum zones are near the primitive circle and minimum zones are clustering around the YZ plane, and Vs_1 polarization is parallel to foliation (XY plane; Figure 11a). While in the post-melt (melt frozen) condition, P-wave's minimum zone is sub-parallel to YZ plane to Z direction, moreover, S-wave anisotropy and two shear wave velocity figures' high value (or low value) zones are cross-like, consequently, similar to P-wave, Vs_1 polarization is also disturbed but the general directions are not influenced (Figure 11a). The syn-melt condition is different to the previous two conditions (Figure 11a): the first three figures' (Vp, AVs, and Vs_1) high-value areas are parallel and close to

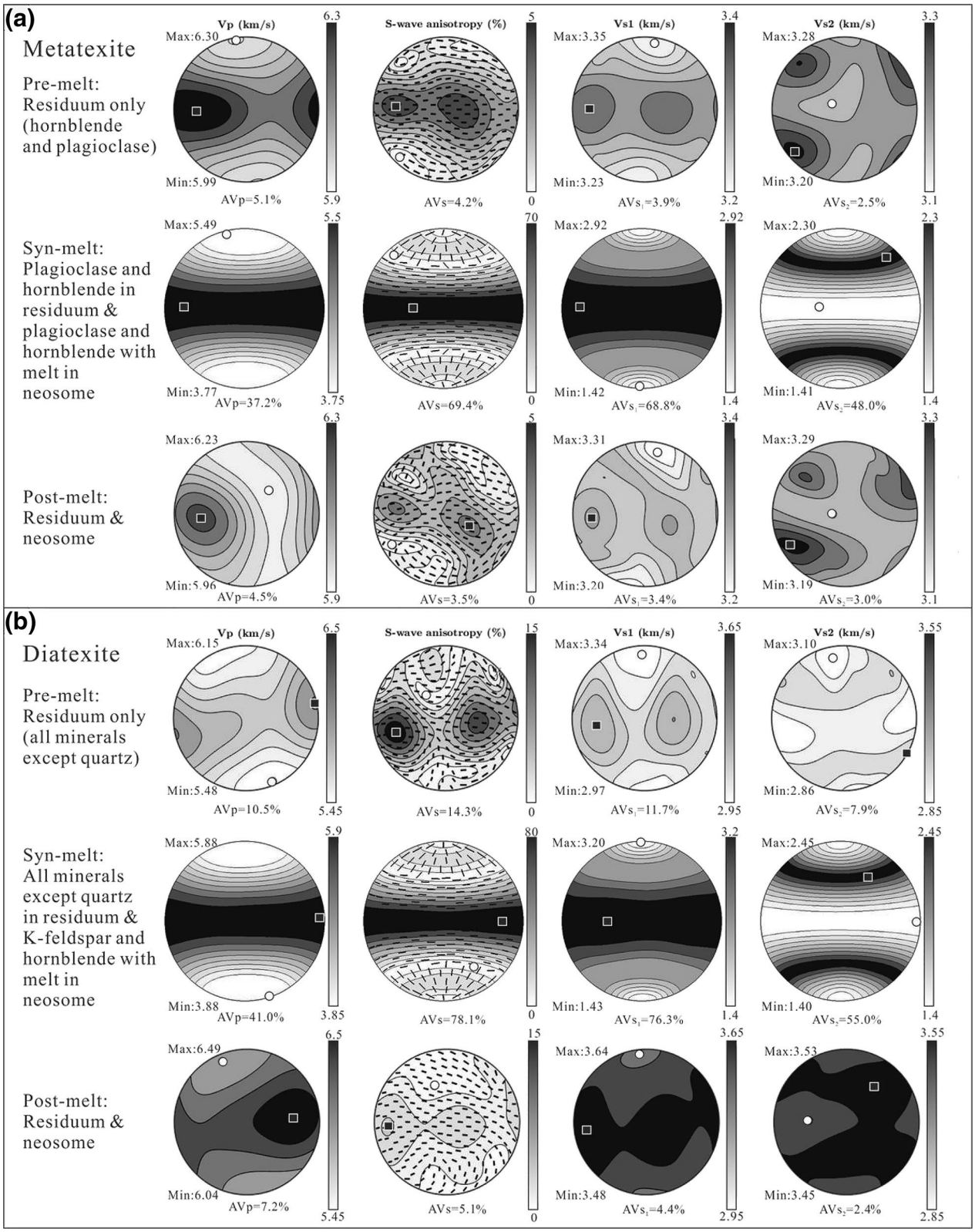

Figure 11. Seismic properties in the pre-melt, syn-melt, and post-melt conditions of the metatexite (a) and diatexite (b) in Daqingshan area. From left to right are 3-D distributions of P-wave velocities (Vp), S-wave anisotropy with orientations of fast shear wave polarization plane, fast and slow S-wave velocities (Vs_1 and Vs_2), separately. Black square: maximum value; white circle: minimum value. Scale migmatite's pre- and post-melt conditions are accordant. AVp, maximum Vp anisotropy; AVs, maximum Vs anisotropy; AVs_1, maximum Vs_1 anisotropy; AVs_2, maximum Vs_2 anisotropy.

Table 3
Seismic Velocities, Anisotropies, and Velocity Ratios of Anatectic Migmatites in Different Melting Conditions (Pre-Melt: Residuum Domain Only; Syn-Melt: Residuum and Crystallized Minerals in Leucosome/Melanosome; Post-Melt: Residuum and Leucosome/Melanosome Domains)

Rock type	Condition	Vp_max (km/s)	Vp_min (km/s)	Vs_1_max (km/s)	Vs_1_min (km/s)	Vs_2_max (km/s)	Vs_2_min (km/s)	Max Vp anisotropy	Max Vs anisotropy	Max Vs_1 anisotropy	Max Vs_2 anisotropy	Vp/Vs_1 max	Vp/Vs_1 min	Vp/Vs_2 max	Vp/Vs_2 min
Metatexite	Pre-melt	6.30	5.99	3.35	3.23	3.28	3.20	5.1	4.2	3.9	2.5	1.89	1.83	1.96	1.85
	Syn-melt	5.49	3.77	2.92	1.42	2.30	1.41	37.2	69.4	68.8	48.0	2.66	1.68	3.88	1.89
	Post-melt	6.23	5.96	3.31	3.20	3.29	3.19	4.5	3.5	3.4	3.0	1.89	1.80	1.95	1.84
Diatexite	Pre-melt	6.15	5.48	3.34	2.97	3.10	2.86	10.5	14.3	11.7	7.9	1.94	1.74	2.15	1.82
	Syn-melt	5.88	3.88	3.20	1.43	2.45	1.40	41.0	78.1	76.3	55.0	2.73	1.62	4.22	1.84
	Post-melt	6.49	6.04	3.64	3.48	3.53	3.45	7.2	5.1	4.4	2.4	1.81	1.72	1.87	1.74

XY plane, Vs_1 polarization is parallel to XY plane in high-value area but randomly in low-value area, Vs_2's high-value zones are shown as girdles along the ~45° direction to X axis.

In the diatexite, the magnitude of all seismic velocity data is lower, while all anisotropic and Vp/Vs data are higher in the pre- than post-melt condition, the data in the syn-melt condition is similar to the metatexite (Table 3). Although the selected minerals in the three conditions are different, the diatexite's seismic properties do not vary a lot between the pre- and post-melt conditions (Figure 11b). The felsic mineral dominant residuum domain has the maximum Vp oriented approximately parallel to lineation, while its minimum Vp direction is slightly inclined (~10°) relative to the foliation, this direction is coincided with the fast biotite (010) direction (Figure S1; Ivankina et al., 2017). S-wave anisotropy's two maximum clusters are almost in symmetry by YZ plane, the Vs_1 polarization is mostly normal except in the lower part of seismic figures that are subvertical to XY plain. Vs_1 also have two maximum clusters parallel to the XY plane, Vs_2 maximum zones are around the base circle, ~45° to X or Z direction and the minimum zones are around the X or Z direction. For the post-melt condition, the distribution of Vp is similar to residuum. A higher S-wave anisotropy (AVs) zone is distributed along the foliation plane and the Vs_1 distribution and polarization in the high anisotropy zones tends to parallel to XY plane. The maximum Vs_2 zone is similar to the residuum and minimum zone is along the YZ plane. The syn-melt condition is also similar to the metatexite (Figure 11b).

6.3. Seismic Properties of the Lower Crust at Different Conditions

The calculated seismic signals give valuable information to infer changes in response to the geological evolution (i.e., state at different conditions). We examine the changes in magnitude of seismic properties for each of the different conditions and discuss these in the light of the literature.

For seismic velocity magnitude, there is a clear correlation between the existence of hornblende and fast Vp. In the metatexite Vp is faster than domains that exhibit low percentage of hornblende (i.e., pre-melt conditions in the metatexite; Tables 3 and 4 and Figure 11; Lloyd et al., 2011; Tatham et al., 2008). As a result, for the pre-melt condition, the metatexite has higher seismic velocities than the diatexite. For syn-melt conditions, the seismic velocities decrease (Table 3). Typically, larger melt fractions lead to greater seismic velocity reduction (Hammond & Humphreys, 2000; Lee et al., 2017). However, in this case study, the metatexite with a lower melt fraction has a greater reduction in seismic velocity (Tables 3 and 4). The main reason for this apparent contradiction is the fact that in the residuum of the diatexite, biotite is relatively abundant (9.1%) and is crystallographically aligned (see Figure S1). This results in a biotite-dependent increase in seismic velocity for both Vs and the seismic anisotropies (Tables 1 and 3; Aleksandrov & Ryzhova, 1961; Barruol & Mainprice, 1993), and counteracts the influence of melt.

In addition, regardless of the different melt fractions and distributions, the two migmatites have similar seismic values (Figure 11); their profiles are also similar to results produced for 20% melt distributed as oblate ellipsoids by Lee et al. (2017). Our predicted maximum shear wave velocity in the two migmatites is consistent with geophysical simulations that show Vs is usually lowest in depth of 20–30 km, due to the existence of melt (Caldwell et al., 2009; Ferri et al., 2016; Hacker et al., 2014).

After the melt crystallizes, the seismic velocities of the two migmatites increase (Tables 3 and 4 and Figure 11). The addition of felsic frozen melt increases the metatexite's P-wave velocity, and the dominant hornblende in the final diatexite increases the seismic velocities (Lloyd et al., 2011; Tatham et al., 2008). By observing seismic velocity distribution (except for the Vs_2) there is a striking change in the pattern of seismic velocities of the metatexite at the post-melt condition relative to the pre-melt condition (Figure 11a). Since K-feldspar is the dominant mineral in the neosome (and second largest percentage in the whole rock) while little is present in the residuum, it is probably the key factor responsible for the observed seismic signals. For the diatexite, although modal contents in the residuum (dominant in the pre-melt condition) and neosome

Table 4
Seismic Signatures of Two Migmatites in Different Melting Periods

	Seismic characteristics		
Rock type	Pre-melt	Syn-melt	Post-melt (compare to pre-melt)
Metatexite	Hornblende leads to higher P-wave velocities.	Obvious lower seismic velocities and higher maximum Vp/Vs ratio, seismic anisotropies have a huge increase. All seismic figures have extremely changes, comparing to the pre- and post-melt conditions.	Vp, AVs and Vs_1 parameters decreased, Vp/Vs kept similar values to residuum, most seismic figures changed with crystallized neosome added.
Diatexite	Dominant felsic minerals lead to lower seismic velocities, biotite leads to higher seismic anisotropies.	Similar to the metatexite.	Seismic velocities and anisotropies were decreased, Vp/Vs were decreased. Minor changes in seismic figures.

(dominant in the post-melt condition) are different, the two conditions have accordant seismic profiles (Figure 11b). Such distribution is likely attributed to biotite in residuum and hornblende in neosome (Kern et al., 2009; Lloyd et al., 2011).

Within the diatexite, seismic anisotropy is strongly related to the presence and alignment of the biotite. Within the residuum biotite accounts for higher seismic anisotropies than that in metatexite domains (Tables 3 and 4 and Figure 11; Ferré et al., 2014; Lloyd et al., 2011). Once in the melt present (syn-melt) condition, both migmatite seismic anisotropies are much greater (Tables 3 and 4 and Figure 11). Almqvist et al. (2015) and Ferri et al. (2016) conducted experiments measuring seismic anisotropy at high temperatures (>700 °C) and the AVp values could be as high as 15%–20%. In this case study, however, even the minimum seismic anisotropy could be as high as 37%. For AVs, the value is coincided with Lee et al. (2017)'s result in migmatitic samples. Regardless of different melt fractions and distributions, in the syn-melt conditions, either melt-injection (metatexite) or in-situ melting (diatexite) lead to extreme-high seismic anisotropies, and Vs_1 polarization parallel to foliation, that is, melt shape alignment.

After melt crystallization, the magnitude of the two migmatites' seismic anisotropies decrease markedly (Tables 3 and 4), following suggestions that decreasing temperature and felsic melt crystallization is expected to decrease seismic anisotropy (Ferri et al., 2016; Lee et al., 2017). AVs anisotropy of the metatexite and diatexite in the post-melt condition's distribution are similar in pattern to the pre-melt conditions (Figure 11).

Generally, if there is little difference in modal content, the Vp/Vs ratios in the migmatites are similar in the non-melt conditions before and after migmatization (Tables 3 and 4). In the syn-melt condition, however maximum Vp/Vs ratios are high and it is even higher in the diatexite (Table 3). A similarly high Vp/Vs (e.g., >2) has been considered in the literature as a signature of partially molten crust (Ferri et al., 2016; Hacker et al., 2014; Julià et al., 2005; Nabelek et al., 2009; Xie et al., 2013). For example, Hacker et al. (2014) conclude that lower crustal rocks with greater partial melt presence have higher Vp/Vs ratios. This is in accordance with the presented data: diatexites that are melt-dominated in the syn-melt condition, exhibit high Vp/Vs ratios (2.73–4.22 for maximum values; Table 3).

7. Conclusions

Our case study investigates the microstructural and crystallographic evolution of typical crustal, medium pressure migmatites. It enables us to identify the active deformation mechanisms, their rheology and seismic characteristics. Using the differences between different domains of the rock, we determine the likely characteristics of lower crust deformation at high temperatures both at solid state, during melt presence and after a migmatization event.

At pre-melt conditions, the tonalitic host rock deforms by dislocation creep at high temperature (>700 °C) including GBM recrystallization where the phases governing the deformation behavior are hornblende and plagioclase. Hence at these conditions the rheology would show a power-law stress-strain rate relationship. Seismic signatures of these rocks are characterized by high P-wave velocity.

At melt present conditions and melt percentages above 10% produced either by in situ partial melting or through injection of externally derived melt, deformation is dominantly consumed by the melt phase, leaving the residuum and floating phenocrysts and residuum-remnants largely in a rigid state. Rheologically this rock has a significantly lower viscosity than its non-melt counterpart and a rheological behavior approaching Newtonian flow. The seismic properties are characterized by lower seismic velocities, higher maximum Vp/Vs ratios and extremely high seismic anisotropies, regardless of different melt fractions and distributions. High melt fraction coincides with high maximum Vp/Vs ratio.

At the post-melt lower crustal condition, the previous felsic melt in the syn-melt condition crystallized as coarse-grained material. Natural examples of such rocks suggest that even though ductile deformation may continue the bulk strain taken up by the "frozen" migmatite is low. Solid state deformation is also dominated by high temperature dislocation creep resulting in a power-law creep behavior. In these rocks the microstructures are well equilibrated (i.e., frequent equilibrium triple junctions), hence high temperature, low strain grain boundary adjustment at high temperatures commonly referred to as annealing must play a major role in the post-migmatization period. Locally some strain localization within, for example, the biotite rich, softer diatexite's residuum may be seen. Migmatites with "frozen felsic melt" (i.e., post-melt condition) exhibit significantly lower seismic velocities, anisotropies, and maximum Vp/Vs ratios than the signatures of the melt present condition. If a migmatite with crystallized leucocratic domains has an overall similar modal mineral content to its residuum, it will show similar seismic signatures as its pre-melt counterpart.

Our study shows that both the rheology and seismic properties of migmatites are significantly and distinctly different at syn-melt conditions than at pre- and post-melt conditions. Consequently, our findings need to be considered in future research focused on both lithospheric rheology and seismic velocity properties.

Data Availability Statement

All data and scripts are available via the DOI https://doi.pangaea.de/10.1594/PANGAEA.907560

Acknowledgments
This project was financially supported by the National Natural Science Foundation of China (Grant No. 41772212, 41872215, 41230206), academic scholarship and oversea academic communication funding project of Jilin University, China Scholarship Council (Grant No. 201708250002), Taishan Scholars (Grant No. ts20190918), Qingdao Leading innovation talents project (Grant No. 19-3-2-19-zhc), and Zhufeng Project funded by Ocean University of China together. Y. Shao is grateful to Liene Spruzeniece and Uvana Meek, Macquarie University for their help with SEM-based EBSD analysis, and to Duo Zhang from College of Earth Sciences, Jilin University, Jonathan Griffin from Department of Geology, University of Otago for proofreading and language help. We are also grateful to Bo Zhang, Bob Miller, Rüdiger Kilian, and two anonymous reviewers for their valuable suggestions, as well as Editor Ulrich Faul for paper handling.

References

Aleksandrov, K., Alchikov, U., Belikov, B., Zaslavskii, B., & Krupnyi, A. (1974). Velocities of elastic waves in minerals at atmospheric pressure and increasing precision of elastic constants by means of EVM [in Russian]. *Izvestiya Akademii Nauk USSR, Seriya Geologicheskaya*, *10*, 15–24.

Aleksandrov, K., & Ryzhova, T. (1961). Elastic properties of rock-forming minerals II: Layered silicates. *Bulletin of the Academy of Sciences of the USSR Geophysics Series, English translation*, *12*, 1165–1168.

Almqvist, B. S. G., & Mainprice, D. (2017). Seismic properties and anisotropy of the continental crust: Predictions based on mineral texture and rock microstructure. *Reviews of Geophysics*. https://doi.org/10.1002/2016rg000552

Almqvist, B. S. G., Misra, S., Klonowska, I., Mainprice, D., & Majka, J. (2015). Ultrasonic velocity drops and anisotropy reduction in mica-schist analogues due to melting with implications for seismic imaging of continental crust. *Earth and Planetary Science Letters*, *425*, 24–33. https://doi.org/10.1016/j.epsl.2015.05.039

Barker, F., & Arth, J. G. (1976). Generation of trondhjemitic-tonalitic liquids and Archean bimodal trondhjemite-basalt suites. *Geology*, *4*(10), 596–600.

Barker, F., Arth, J. G., & Hudson, T. (1981). Tonalites in crustal evolution. *Philosophical Transactions of the Royal Society of London - Series A: Mathematical and Physical Sciences*, *301*(1461), 293–303.

Barruol, G., & Mainprice, D. (1993). A quantitative evaluation of the contribution of crustal rocks to the shear-wave splitting of teleseismic SKS waves. *Physics of the Earth and Planetary Interiors*, *78*(3-4), 281–300.

Berger, A., & Stünitz, H. (1996). Deformation mechanisms and reaction of hornblende: examples from the Bergell tonalite (Central Alps). *Tectonophysics*, *257*, 149–174.

Bestmann, M., & Prior, D. J. (2003). Intragranular dynamic recrystallization in naturally deformed calcite marble: diffusion accommodated grain boundary sliding as a result of subgrain rotation recrystallization. *Journal of Structural Geology*, *25*(10), 1597–1613. https://doi.org/10.1016/s0191-8141(03)00006-3

Bürgmann, R., & Dresen, G. (2008). Rheology of the lower crust and upper mantle: Evidence from Rock Mechanics, Geodesy, and Field Observations. *Annual Review of Earth and Planetary Sciences*, *36*(1), 531–567. https://doi.org/10.1146/annurev.earth.36.031207.124326

Burg, J. P., & Vigneresse, J. L. (2002). Non-linear feedback loops in the rheology of cooling-crystallizing felsic magma and heating-melting felsic rock. *Geological Society, London, Special Publications*, *200*(1), 275–292.

Burov, E. B., & Diament, M. (1995). The effective elastic thickness (T e) of continental lithosphere: What does it really mean?. *Journal of Geophysical Research: Solid Earth*, *100*(B3), 3905–3927.

Busch, W., Schneider, C., & Mehnert, K. R. (1974). Initial melting at grain boundaries. Part II: Melting in rocks of granodioritic, quartzdioritic and tonalitic composition. *Neues Jahrbuch für Mineralogie*, *8*, 345–370

Cai, J., Liu, P., Liu, F., Liu, J., Wang, F., & Shi, J. (2013). Genetic mineralogy and metamorphic evolution of Al-rich gneisses in the Shiguai area, Daqingshan-Wulashan metamorphic complex belt [in Chinese with English abstract]. *Acta Petrologica Sinica*, *29*(2), 437–461.

Cai, J., Liu, F., Liu, P., Liu, C., Wang, F., & Shi, J. (2014). Metamorphic P–T path and tectonic implications of pelitic granulites from the Daqingshan Complex of the Khondalite Belt, North China Craton. *Precambrian Research*, *241*, 161–184. https://doi.org/10.1016/j.precamres.2013.11.012

Cai, J., Liu, F., Liu, P., Shi, J., & Liu, J. (2013). Petrogenesis and metamorphic P-T conditions of garnet-spinel-biotite-bearing paragneiss in Danangou area, Daqingshan-Wulashan metamorphic complex belt [in Chinese with English abstract]. *Acta Petrologica Sinica*, *29*(7), 2313–2328.

Caldwell, W. B., Klemperer, S. L., Rai, S. S., & Lawrence, J. F. (2009). Partial melt in the upper-middle crust of the northwest Himalaya revealed by Rayleigh wave dispersion. *Tectonophysics*, *477*(1-2), 58–65. https://doi.org/10.1016/j.tecto.2009.01.013

Champallier, R., Bystricky, M., & Arbaret, L. (2008). Experimental investigation of magma rheology at 300 MPa: From pure hydrous melt to 76 vol.% of crystals. *Earth and Planetary Science Letters*, *267*(3-4), 571–583. https://doi.org/10.1016/j.epsl.2007.11.065

Cooper, R. F., & Kohlstedt, D. L. (1984). Solution-precipitation enhanced diffusional creep ofpartially molten olivine-basalt aggregates during hot-pressing. *Tectonophysics*, *107*, 207–233.

Corona-Chávez, P., Poli, S., & Bigioggero, B. (2006). Syn-deformational migmatites and magmatic-arc metamorphism in the Xolapa Complex, southern Mexico. *Journal of Metamorphic Geology*, *24*(3), 169–191.

Cyprych, D., Piazolo, S., & Almqvist, B. S. G. (2017). Seismic anisotropy from compositional banding in granulites from the deep magmatic arc of Fiordland, New Zealand. *Earth and Planetary Science Letters*, *477*, 156–167. https://doi.org/10.1016/j.epsl.2017.08.017

Dallain, C., Schulmann, K., & Ledru, P. (1999). Textural evolution in the transition from subsolidus annealing to melting process, Velay Dome, French Massif Central. *Journal of Metamorphic Geology*, *17*, 61–74.

Danner, T., Hjorth Jakobsen, U., & Geiker, M. R. (2019). Mineralogical sequence of self-healing products in cracked marine concrete. *Minerals*, *9*(5), 284.

Dell'Angelo, L. N., & Tullis, J. (1988). Experimental deformation of partially melted granitic aggregates. *Journal of Metamorphic Geology*, *6*, 495–515.

Díaz Aspiroz, M., Lloyd, G. E., & Fernández, C. (2007). Development of lattice preferred orientation in clinoamphiboles deformed under low-pressure metamorphic conditions. A SEM/EBSD study of metabasites from the Aracena metamorphic belt (SW Spain). *Journal of Structural Geology*, *29*(4), 629–645. https://doi.org/10.1016/j.jsg.2006.10.010

Dong, C., Wan, Y., Wilde, S. A., Xu, Z., Ma, M., Xie, H., & Liu, D. (2014). Earliest Paleoproterozoic supracrustal rocks in the North China Craton recognized from the Daqingshan area of the Khondalite Belt: Constraints on craton evolution. *Gondwana Research*, *25*(4), 1535–1553

Elías-Herrera, M., & Ortega-Gutiérrez, F. (2002). Caltepec fault zone: An Early Permian dextral transpressional boundary between the Proterozoic Oaxacan and Paleozoic Acatlán complexes, southern Mexico, and regional tectonic implications. *Tectonics*, *21*(3), 4–1. https://doi.org/10.1029/2000tc001278

Ferré, E. C., Gébelin, A., Conder, J. A., Christensen, N., Wood, J. D., & Teyssier, C. (2014). Seismic anisotropy of the Archean crust in the Minnesota River Valley, Superior Province. *Geophysical Research Letters*, *41*(5), 1514–1522.

Ferri, F., Burlini, L., & Cesare, B. (2016). Effect of partial melting on Vp and Vs in crustal enclaves from Mazarrón (SE Spain). *Tectonophysics*, *671*, 139–150. https://doi.org/10.1016/j.tecto.2015.12.030

Flinn, D. (1969). Grain contacts in crystalline rocks. *Lithos*, *3*, 361–370.

Franěk, J., Schulmann, K., Lexa, O., Ulrich, S., Štípská, P., Haloda, J., & Týcová, P. (2011). Origin of felsic granulite microstructure by heterogeneous decomposition of alkali feldspar and extreme weakening of orogenic lower crust during the Variscan orogeny. *Journal of Metamorphic Geology*, *29*(1), 103–130. https://doi.org/10.1111/j.1525-1314.2010.00911.x

Getsinger, A. J., & Hirth, G. (2014). Amphibole fabric formation during diffusion creep and the rheology of shear zones. *Geology*, *42*(6), 535–538. https://doi.org/10.1130/g35327.1

Gómez Barreiro, J., Lonardelli, I., Wenk, H. R., Dresen, G., Rybacki, E., Ren, Y., & Tomé, C. N. (2007). Preferred orientation of anorthite deformed experimentally in Newtonian creep. *Earth and Planetary Science Letters*, *264*(1-2), 188–207. https://doi.org/10.1016/j.epsl.2007.09.018

Gong, W., Hu, J., Wu, S., Chen, H., Qu, H., Li, Z., et al. (2014). Possible southwestward extrusion of the Ordos Block in the Late Paleoproterozoic: Constraints from kinematic and geochronologic analysis of peripheral ductile shear zones. *Precambrian Research*, *255*, 716–733. https://doi.org/10.1016/j.precamres.2014.05.001

Guernina, S., & Sawyer, E. W. (2003). Large-scale melt-depletion in granulite terranes: an example from the Archean Ashuanipi Subprovince of Quebec. *Journal of Metamorphic Geology*, *21*, 181–201.

Guo, J., Peng, P., Chen, Y., Jiao, S., & Windley, B. F. (2012). UHT sapphirine granulite metamorphism at 1.93–1.92Ga caused by gabbronorite intrusions: Implications for tectonic evolution of the northern margin of the North China Craton. *Precambrian Research*, *222-223*, 124–142. https://doi.org/10.1016/j.precamres.2011.07.020

Hacker, B. R., Ritzwoller, M. H., & Xie, J. (2014). Partially melted, mica-bearing crust in Central Tibet. *Tectonics*, *33*, 1408–1424.

Hammond, W. C., & Humphreys, E. D. (2000). Upper mantle seismic wave velocity: Effects of realistic partial melt geometries. *Journal of Geophysical Research: Solid Earth*, *105*(B5), 10975–10986. https://doi.org/10.1029/2000jb900041

Hansen, L. N., Zhao, Y. H., Zimmerman, M. E., & Kohlstedt, D. L. (2014). Protracted fabric evolution in olivine: Implications for the relationship among strain, crystallographic fabric, and seismic anisotropy. *Earth and Planetary Science Letters*, *387*, 157–168. https://doi.org/10.1016/j.epsl.2013.11.009

Hasalová, P., Schulmann, K., Lexa, O., Štípská, P., Hrouda, F., Ulrich, S., et al. (2008). Origin of migmatites by deformation-enhanced melt infiltration of orthogneiss: A new model based on quantitative microstructural analysis. *Journal of Metamorphic Geology*, *26*(1), 29–53.

Hill, R. (1952). The elastic behaviour of a crystalline aggregate. *Proceedings of the Physical Society A*, *65*, 349–354.

Holtzman, B. K., & Kendall, J. M. (2010). Organized melt, seismic anisotropy, and plate boundary lubrication. *Geochemistry, Geophysics, Geosystems*, *11*(12). https://doi.org/10.1029/2010gc003296

Hu, Z.P., Zhang, Y.S., Hu, R., Wang, J., Siebel, W., & Chen, F. (2016). Amphibole-bearing migmatite in North Dabie, eastern China: Water-fluxed melting of the orogenic crust. *Journal of Asian Earth Sciences*, *125*, 100–116.

Imon, R., Okudaira, T., & Kanagawa, K. (2004). Development of shape- and lattice-preferred orientations of amphibole grains during initial cataclastic deformation and subsequent deformation by dissolution–precipitation creep in amphibolites from the Ryoke metamorphic belt, SW Japan. *Journal of Structural Geology*, *26*(5), 793–805. https://doi.org/10.1016/j.jsg.2003.09.004

Ishii, K., Kanagawa, K., Shigematsu, N., & Okudaira, T. (2007). High ductility of K-feldspar and development of granitic banded ultramylonite in the Ryoke metamorphic belt, SW Japan. *Journal of Structural Geology*, *29*(6), 1083–1098. https://doi.org/10.1016/j.jsg.2007.02.008

Ivankina, T. I., Zel, I. Y., Lokajicek, T., Kern, H., Lobanov, K. V., & Zharikov, A. V. (2017). Elastic anisotropy of layered rocks: Ultrasonic measurements of plagioclase-biotite-muscovite (sillimanite) gneiss versus texture-based theoretical predictions (effective media modeling). *Tectonophysics*, *712*, 82–94.

Jackson, J. (2002). Strength of the continental lithosphere: time to abandon the jelly sandwich? *GSA Today*, *12*, 4–9.

Ji, S., Jiang, Z., Rybacki, E., Wirth, R., Prior, D., & Xia, B. (2004). Strain softening and microstructural evolution of anorthite aggregates and quartz–anorthite layered composites deformed in torsion. *Earth and Planetary Science Letters*, *222*(2), 377–390. https://doi.org/10.1016/j.epsl.2004.03.021

Jin, W., Li, S., & Liu, X. (1991). A study on characteristics of early Precambrian high-grade metamorphic rock series and their metamorphic dynamics [in Chinese with English abstract]. *Acta Petrologica Sinica*, *4*, 27–35.

Jin, W., Li, S., & Liu, X. (1992). Early Precambrian metamorphic rocks and early earth crust evolution in Daqingshan, Inner Mongolia [in Chinese with English abstract]. *Journal of Changchun University of Earth Sciences*, *22*(3), 281–289.

Johannes, W., & Gupta, L.N. (1982). Origin and evolution of a migmatite. *Contributions to Mineralogy and Petrology*, *79*(2), 114–123.

Julià, J., Mancilla, F., & Morales, J. (2005). Seismic signature of intracrustal magmatic intrusions in the Eastern Betics (Internal Zone), SE Iberia. *Geophysical Research Letters*, *32*(16).

Kern, H., Mengel, K., Strauss, K., Ivankina, T., Nikitin, A., & Kukkonen, I. (2009). Elastic wave velocities, chemistry and modal mineralogy of crustal rocks sampled by the Outokumpu scientific drill hole: Evidence from lab measurements and modeling. *Physics of the Earth and Planetary Interiors*, *175*(3-4), 151–166.

Kretz, R. (1983). Symbols for rock-forming minerals. *American Mineralogist*, *68*(1-2), 277–279.

Kriegsman, L. M. (2001). Partial melting, partial melt extraction and partial back reaction in anatectic migmatites. *Lithos*, *56*, 75–96.

Kriegsman, L. M., & Hensen, B. J. (1998). Back reaction between restite and melt implications for geothermobarometry and pressure-temperature paths. *Geology*, *26*(12), 1111–1114.

Kruse, R., Stünitz, H., & Kunze, K. (2001). Dynamic recrystallization processes in plagioclase porphyroclasts. *Journal of Structural Geology*, *23*, 1781–1802.

Lamarque, G., Bascou, J., Maurice, C., Cottin, J.-Y., Riel, N., & Ménot, R.-P. (2016). Microstructures, deformation mechanisms and seismic properties of a Palaeoproterozoic shear zone: The Mertz shear zone, East-Antarctica. *Tectonophysics*, *680*, 174–191. https://doi.org/10.1016/j.tecto.2016.05.011

Law, R. D. (1990). Crystallographic fabrics: a selective review of their applications to research in structural geology. *Geological Society, London, Special Publications*, *54*(1), 335–352. https://doi.org/10.1144/gsl.sp.1990.054.01.30

Lee, A. L., Walker, A. M., Lloyd, G. E., & Torvela, T. (2017). Modeling the impact of melt on seismic properties during mountain building. *Geochemistry, Geophysics, Geosystems*, *18*, 1–21. https://doi.org/10.1029/2009GC002637

Lejeune, A. M., & Richet, P. (1995). Rheology of crystal-bearing silicate melts: An experimental study at high viscosities. *Journal of Geophysical Research: Solid Earth*, *100*(B3), 4215–4229. https://doi.org/10.1029/94jb02985

Lloyd, G. E., Butler, R. W. H., Casey, M., Tatham, D., & Mainprice, D. (2011). Constraints on the seismic properties of the middle and lower continental crust. *Geological Society, London, Special Publications*, *360*(1), 7–32.

Lobjoie, C., Lin, W., Trap, P., Goncalves, P., Li, Q., Marquer, D., et al. (2018). Ultra-high temperature metamorphism recorded in Fe-rich olivine-bearing migmatite from the Khondalite Belt, North China Craton. *Journal of Metamorphic Geology*, *36*(3), 343–368.

Mainprice, D. (1990). A FORTRAN program to calculate seismic anisotropy from the lattice preferred orientation of minerals. *Computers & Geosciences*, *16*(3), 385–393.

Mainprice, D., Bachmann, F., Hielscher, R., Schaeben, H., & Lloyd, G. E. (2014). Calculating anisotropic piezoelectric properties from texture data using the MTEX open source package. *Geological Society, London, Special Publications*, *409*(1), 223–249. https://doi.org/10.1144/sp409.2

Mainprice, D., Hielscher, R., & Schaeben, H. (2011). Calculating anisotropic physical properties from texture data using the MTEX open-source package. *Geological Society, London, Special Publications*, *360*(1), 175–192. https://doi.org/10.1144/sp360.10

Marshall, D. B., & McLaren, A. C. (1977). Deformation mechanisms in experimentally deformed plagioclase feldspars. *Physics and Chemistry of Minerals*, *1*, 351–370.

Martelat, J. E., Schulmann, K., Lardeaux, J. M., Nicollet, C., & Cardon, H. (1999). Granulite microfabrics and deformation mechanisms in southern Madagascar. *Journal of Structural Geology*, *21*, 671–687.

Ma, M., Wan, Y., Santosh, M., Xu, Z., Xie, H., Dong, C., et al. (2012). Decoding multiple tectonothermal events in zircons from single rock samples: SHRIMP zircon U–Pb data from the late Neoarchean rocks of Daqingshan, North China Craton. *Gondwana Research*, *22*(3–4), 810–827. http://dx.doi.org/10.1016/j.gr.2012.02.020

Ma, M., Wan, Y., Xu, Z., Liu, S., Xie, H., Dong, C., & Liu, D. (2012). Late Paleoproterozoic K-feldspar pegmatite vein in the Daqingshan area, North China Craton: SHRIMP age and Hf composition of zircons. *Geological Bulletin of China*, *31*(6), 825–833.

Maxeiner, R. O., Ashton, K., Card, C. D., Morelli, R. M., & Knox, B. (2017). A field guide to naming migmatites and their textures, with Saskatchewan examples. *Summary of Investigations*, *2*, 2017-4.

McSkimin, H., Andreatch, P., Jr, & Thurston, R. (1965). Elastic moduli of quartz versus hydrostatic pressure at 25 and− 195.8 C. *Journal of Applied Physics*, *36*(5), 1624–1632.

Menegon, L., Piazolo, S., & Pennacchioni, G. (2011). The effect of Dauphiné twinning on plastic strain in quartz. *Contributions to Mineralogy and Petrology*, *161*(4), 635–652. https://doi.org/10.1007/s00410-010-0554-7

Miranda, E. A., & Klepeis, K. A. (2016). The interplay and effects of deformation and crystallized melt on the rheology of the lower continental crust, Fiordland, New Zealand. *Journal of Structural Geology*, *93*, 91–105. https://doi.org/10.1016/j.jsg.2016.09.007

Morales, L. F. G., & Tommasi, A. (2011). Composition, textures, seismic and thermal anisotropies of xenoliths from a thin and hot lithospheric mantle (Summit Lake, southern Canadian Cordillera). *Tectonophysics*, *507*(1-4), 1–15. https://doi.org/10.1016/j.tecto.2011.04.014

Nabelek, J., Hetenyi, G., Vergne, J., Sapkota, S., Kafle, B., Jiang, M., et al. (2009). Underplating in the Himalaya-Tibet collision zone revealed by the Hi-CLIMB experiment. *Science*, *325*(5946), 1371–1374. https://doi.org/10.1126/science.1167719

Olsen, S. N. (1977). Origin of the Baltimore gneiss migmatites at Piney Creek, Maryland. *Geological Society of America Bulletin*, *88*(8), 1089–1101.

Passchier, C. W. (1984). The generation of ductile and brittle shear bands in a low-angle mylonite zone. *Journal of Structural Geology*, *6*(3), 273–281. https://doi.org/10.1016/0191-8141(84)90051-8

Passchier, C. W., & Trouw, R. A. J. (2005). *Microtectonics* (2nd.). Berlin: Springer-verlag.

Paterson, M. S. (2001). A granular flow theory for the deformation of partially molten rock. *Tectonophysics*, *335*, 51–61.

Pearce, M. A., Wheeler, J., & Prior, D. J. (2011). Relative strength of mafic and felsic rocks during amphibolite facies metamorphism and deformation. *Journal of Structural Geology*, *33*(4), 662–675. https://doi.org/10.1016/j.jsg.2011.01.002

Piazolo, S., Bestmann, M., Prior, D. J., & Spiers, C. J. (2006). Temperature dependent grain boundary migration in deformed-then-annealed material: Observations from experimentally deformed synthetic rocksalt. *Tectonophysics*, *427*(1-4), 55–71. https://doi.org/10.1016/j.tecto.2006.06.007

Prakash, A., Piazolo, S., Saha, L., Bhattacharya, A., Pal, D. K., & Sarkar, S. (2018). Deformation behavior of migmatites: insights from microstructural analysis of a garnet–sillimanite–mullite–quartz–feldspar-bearing anatectic migmatite at Rampura–Agucha, Aravalli–Delhi Fold Belt, NW India. *International Journal of Earth Sciences*. https://doi.org/10.1007/s00531-018-1598-6

Prior, D. J., Boyle, A. P., Brenker, F., Cheadle, M. C., Day, A., Lopez, G., et al. (1999). The application of electron backscatter diffraction and orientation contrast imaging in the SEM to textural problems in rocks. *American Mineralogist*, *84*, 1741–1759.

Prior, D. J., Wheeler, J., Peruzzo, L., Spiess, R., & Storey, C. (2002). Some garnet microstructures an illustration of the potential of orientation maps and misorientation analysis in microstructural studies. *Journal of Structural Geology*, *24*, 999–1011.

Rey, P. F., Teyssier, C., & Whitney, D. L. (2009). Extension rates, crustal melting, and core complex dynamics. *Geology*, *37*(5), 391–394.

Rivers, M. L., & Carmichael, I. S. (1987). Ultrasonic studies of silicate melts. *Journal of Geophysical Research: Solid Earth*, *92*(B9), 9247–9270.

Rosenberg, C. L., & Handy, M. R. (2005). Experimental deformation of partially melted granite revisited: implications for the continental crust. *Journal of Metamorphic Geology*, *23*(1), 19–28. https://doi.org/10.1111/j.1525-1314.2005.00555.x

Rosenberg, C. L., & Stünitz, H. (2003). Deformation and recrystallization of plagioclase along a temperature gradient an example from the Bergell tonalite. *Journal of Structural Geology*, *25*, 389–408.

Rudnick, R. L., & Fountain, D. M. (1995). Nature and composition of the continental crust: a lower crustal perspective. *Reviews of Geophysics*, *33*(3), 267–309.

Rybacki, E., & Dresen, G. (2004). Deformation mechanism maps for feldspar rocks. *Tectonophysics*, *382*(3-4), 173–187. https://doi.org/10.1016/j.tecto.2004.01.006

Santosh, M., Sajeev, K., Li, J. H., Liu, S. J., & Itaya, T. (2009). Counterclockwise exhumation of a hot orogen: The Paleoproterozoic ultrahigh-temperature granulites in the North China Craton. *Lithos*, *110*(1-4), 140–152. https://doi.org/10.1016/j.lithos.2008.12.010

Santosh, M., Tsunogae, T., Li, J. H., & Liu, S. J. (2007). Discovery of sapphirine-bearing Mg–Al granulites in the North China Craton: Implications for Paleoproterozoic ultrahigh temperature metamorphism. *Gondwana Research*, *11*(3), 263–285. https://doi.org/10.1016/j.gr.2006.10.009

Sawyer, E. W. (1996). Melt segregation and magma flow in migmatites: implications for the generation of granite magmas. *Transactions of the Royal Society of Edinburgh-Earth Sciences*, *87*(1), 85–94.

Sawyer, E. W. (1999). Criteria for the recognition of partial melting. *Physics and Chemistry of the Earth*, *24*(3), 269–279.

Sawyer, E. W. (2001). Melt segregation in the continental crust: distribution and movement of melt in anatectic rocks. *Journal of Metamorphic Geology*, *19*, 291–309.

Sawyer, E. W. (2008). Atlas of migmatites (Vol. 9). Ottawa: NRC Research Press.

Sawyer, E. W. (2014). The inception and growth of leucosomes: microstructure at the start of melt segregation in migmatites. *Journal of Metamorphic Geology*, *32*(7), 695–712. https://doi.org/10.1111/jmg.12088

Sawyer, E. W., & Brown, M. (Eds.) (2008). Working with migmatites (Vol. *38*). Mineralogical Assn of Canada.

Sawyer, E. W., Cesare, B., & Brown, M. (2011). When the Continental Crust Melts. *Elements*, *7*(4), 229–234. https://doi.org/10.2113/gselements.7.4.229

Schilling, F. R., & Partzsch, G. M. (2001). Quantifying partial melt fraction in the crust beneath the central Andes and the Tibetan Plateau. *Physics and Chemistry of the Earth, Part A: Solid Earth and Geodesy*, *26*(4), 239–246.

Smith, J. R., Piazolo, S., Daczko, N. R., & Evans, L. (2015). The effect of pre-tectonic reaction and annealing extent on behaviour during subsequent deformation: insights from paired shear zones in the lower crust of Fiordland, New Zealand. *Journal of Metamorphic Geology*, *33*(6), 557–577. https://doi.org/10.1111/jmg.12132

Speer, J. A. (1987). Evolution of magmatic AFM mineral assemblages in granitoid rocks; the hornblende+ melt= biotite reaction in the Liberty Hill Pluton, South Carolina. *American Mineralogist*, *72*(9-10), 863–878.

Stuart, C. A., Daczko, N. R., & Piazolo, S. (2017). Local partial melting of the lower crust triggered by hydration through melt-rock interaction: an example from Fiordland, New Zealand. *Journal of Metamorphic Geology*, *35*(2), 213–230. https://doi.org/10.1111/jmg.12229

Stuart, C. A., Meek, U., Daczko, N. R., Piazolo, S., & Huang, J. X. (2018). Chemical Signatures of Melt–Rock Interaction in the Root of a Magmatic Arc. *Journal of Petrology*, *59*(2), 321–340. https://doi.org/10.1093/petrology/egy029

Tatham, D. J., Lloyd, G. E., Butler, R. W. H., & Casey, M. (2008). Amphibole and lower crustal seismic properties. *Earth and Planetary Science Letters*, *267*(1-2), 118–128. https://doi.org/10.1016/j.epsl.2007.11.042

Trimby, P. W., Drury, M. R., & Spiers, C. J. (2000). Recognising the crystallographic signature of recrystallisation processes in deformed rocks: a study of experimentally deformed rocksalt. *Journal of Structural Geology*, *22*(11-12), 1609–1620.

Tuttle, O. F., & Bowen, N. L. (1958). Origin of Granite in the Light of Experimental Studies in the System $NaA1Si_3O_8$-$KA1Si_3$-H_2O. *Geological Society of America*.

Urai, J. L., Means, W. D., & Lister, G. S. (1986). Dynamic recrystallization of minerals. In Mineral and rock deformation: Laboratory studies (Vol. 36, pp. 161–199). Washington, DC: AGU.

Vanderhaeghe, O. (2001). Melt segregation, pervasive melt migration and magma mobility in the continental crust: the structural record from pores to orogens. *Physics and Chemistry of the Earth, Part A: Solid Earth and Geodesy*, *26*(4), 213–223.

Vanderhaeghe, O. (2009). Migmatites, granites and orogeny: Flow modes of partially-molten rocks and magmas associated with melt/solid segregation in orogenic belts. *Tectonophysics*, *477*(3-4), 119–134.

Vanderhaeghe, O., & Teyssier, C. (2001). Partial melting and flow of orogens. *Tectonophysics*, *342*, 451–472.

Venables, J., & Harland, C. (1973). Electron back-scattering patterns—A new technique for obtaining crystallographic information in the scanning electron microscope. *Philosophical Magazine*, *27*(5), 1193–1200.

Walker, A. M., & Wookey, J. (2012). MSAT—A new toolkit for the analysis of elastic and seismic anisotropy. *Computers & Geosciences*, *49*, 81–90.

Walte, N. P., Bons, P. D., & Passchier, C. W. (2005). Deformation of melt-bearing systems—Insight from in situ grain-scale analogue experiments. *Journal of Structural Geology*, *27*(9), 1666–1679. https://doi.org/10.1016/j.jsg.2005.05.006

Wan, Y., Liu, D., Dong, C., Xu, Z., Wang, Z., Wilde, S. A., et al. (2009). The Precambrian Khondalite Belt in the Daqingshan area, North China Craton: evidence for multiple metamorphic events in the Palaeoproterozoic era. *Geological Society, London, Special Publications*, *323*(1), 73–97.

Wan, Y., Xu, Z., Dong, C., Nutman, A., Ma, M., Xie, H., et al. (2013). Episodic Paleoproterozoic (~2.45, ~1.95 and ~1.85 Ga) mafic magmatism and associated high temperature metamorphism in the Daqingshan area, North China Craton: SHRIMP zircon U–Pb dating and whole-rock geochemistry. *Precambrian Research*, *224*, 71–93. http://dx.doi.org/10.1016/j.precamres.2012.09.014

Warren, J. M., & Hirth, G. (2006). Grain size sensitive deformation mechanisms in naturally deformed peridotites. *Earth and Planetary Science Letters*, *248*, 438–450. https://doi.org/10.1016/j.epsl.2006.06.006

Weinberg, R. F., & Hasalová, P. (2015). Water-fluxed melting of the continental crust: A review. *Lithos*, *212-215*, 158–188. https://doi.org/10.1016/j.lithos.2014.08.021

Weinberg, R. F., Veveakis, E., & Regenauer-Lieb, K. (2015). Compaction-driven melt segregation in migmatites. *Geology*, *43*(6), 471–474.

Wright, S. I., Nowell, M. M., & Field, D. P. (2011). A review of strain analysis using electron backscatter diffraction. *Microscopy and Microanalysis*, *17*(3), 316–329.

Xie, J., Ritzwoller, M. H., Shen, W., Yang, Y., Zheng, Y., & Zhou, L. (2013). Crustal radial anisotropy across Eastern Tibet and the Western Yangtze Craton. *Journal of Geophysical Research: Solid Earth*, *118*(8), 4226–4252. https://doi.org/10.1002/jgrb.50296

Xu, Z., Liu, Z., Yang, Z., Wu, X., & Chen, X. (2007). Structure of metamorphic strata of the khondalite series in the Daqingshan-Wulashan area, central Inner Mongolia, China, and their geodynamic implications [in Chinese with English abstract]. *Geological Bulletin of China*, *26*(5), 526–536.

Xu, Z., Wan, Y., Dong, C., Ma, M., & Liu, D. (2015). Late Neoarchean magmatism identified in Daqingshan, Inner Mongolia: SHRIMP zircon U-Pb dating [in Chinese with English abstract]. *Acta Petrologica Sinica*, *31*(6), 1509–1517.

Yang, Z., Xu, Z., Liu, Z., & Huang, D. (2008). *Geological investigation and research on high-grade metamorphic regions [in Chinese]*. Beijing: Geological Publication House.

Závada, P., Schulmann, K., Konopásek, J., Ulrich, S., & Lexa, O. (2007). Extreme ductility of feldspar aggregates—Melt-enhanced grain boundary sliding and creep failure: Rheological implications for felsic lower crust. *Journal of Geophysical Research*, *112*(B10). https://doi.org/10.1029/2006jb004820

Závada, P., Schulmann, K., Racek, M., Hasalová, P., Petr, J., Weinberg, R. F., et al. (2018). Role of strain localization and melt flow on exhumation of deeply subducted continental crust. *Lithosphere*, *10*(2), 217–238.

Zhao, G. (2007). When did plate tectonics begin on the North China Craton Insights from metamorphism. *Earth Science Frontiers*, *14*(1), 19–32.

Zhao, G., Cawood, P. A., Li, S., Wilde, S. A., Sun, M., Zhang, J., et al. (2012). Amalgamation of the North China Craton: Key issues and discussion. *Precambrian Research*, *222-223*, 55–76. https://doi.org/10.1016/j.precamres.2012.09.016

Zhao, G., & Guo, J. (2012). Precambrian geology of China: preface. *Precambrian Research*, *222*, 1–12.

Zhao, G., Sun, M., Wilde, S. A., & Li, S. (2005). Late Archean to Paleoproterozoic evolution of the North China Craton: key issues revisited. *Precambrian Research*, *136*(2), 177–202.

Zhao, G., Wilde, S. A., Cawood, P. A., & Sun, M. (2002). SHRIMP U–Pb zircon ages of the Fuping Complex: implications for late Archean to Paleoproterozoic accretion and assembly of the North China Craton. *American Journal of Science*, *302*(3), 191–222.